Summer 7-29-2024

Differential River Incision due to Quaternary Faulting on the Río Jemez-Salado System at the Million-Year Timescale

Cameron Reed
The University of New Mexico

Cameron Chavez Reed

Candidate

Earth and Planetary Sciences

Department

This thesis is approved, and it is acceptable in quality and form for publication:

Approved by the Thesis Committee:

Karl Karlstrom , Chairperson

Laura Crossey

Matthew Heizler

DIFFERENTIAL RIVER INCISION DUE TO QUATERNARY FAULTING ON THE RÍO JEMEZ-SALADO SYSTEM AT THE MILLION-YEAR TIMESCALE

by

CAMERON CHAVEZ REED

B.S. ARIZONA STATE UNIVERSITY, EARTH AND SPACE EXPLORATION (GEOLOGICAL SCIENCES), 2021

B.A. ARIZONA STATE UNIVERSITY, SUSTAINABILITY, 2021

THESIS

Submitted in Partial Fulfillment of the
Requirements for the Degree of

Master of Science
Earth and Planetary Sciences

The University of New Mexico
Albuquerque, New Mexico

July 2024

DEDICATION

This thesis and work is dedicated to my lovely partner, Christopher, an amazing baker, gentle and funny soul, and caring cat parent to our children. Thank you for putting up with all my frustrations and supporting me through every stress riddled deadline. I also dedicate this to my wonderful and supportive parents, Jenn and Greg. Without them, I wouldn't have been able to get to where I am today. Thank you, mama and nana, for your tenacious support of my studies and connection to our nuevoméxicano heritage. I am sure my academic skills were hardened by disciplined teachings in the kitchen and a few flying chanclas. Thank you, papa, for cultivating a curiosity and belongingness to the outdoors and natural world including the numerous fishing and hiking trips to the places I study now.

ACKNOWLEDGEMENTS

Huge thanks to everyone who has supported me through my program at UNM in and beyond my research. I thank the New Mexico Geological Society, Geological Society of America, Colorado Scientific Society, and UNM Graduate and Professional Student Association for partially financially supporting this research. I would also like to thank my advisor, Dr. Karl Karlstrom, for guidance navigating research and grad school and for his thoughtful input at every step. Thank you to Dr. Laura Crossey for her insight and support. Thank you, Dr. Matt Heizler and Dr. Julia Ricci, for help in the lab, geochronology work, and advisement through many hours of picking for sanidines. I would like to thank the New Mexico Geochronology Research Laboratory for their expertise and resources contributed to geochronology work. Tephrochronology work could not be done without Nels Iverson at New Mexico Tech. Thank you, Ben Rodriguez, for field and lab assistance along the way.

DIFFERENTIAL RIVER INCISION DUE TO QUATERNARY FAULTING ON THE RÍO JEMEZ-SALADO SYSTEM AT THE MILLION-YEAR TIMESCALE

Cameron Chavez Reed

B.S. Earth and Space Exploration (Geological Sciences)

B.A. Sustainability

M.S. Earth and Planetary Sciences

ABSTRACT

Analysis of long-term average bedrock incision rates along the Río Salado-Jemez system using fluvial terraces can be used to test and quantify the hypothesis that differential river incision reflects Quaternary fault slip during ongoing uplift of the Jemez and Nacimiento Mountains. Terrace flights were correlated from the Arroyo Peñasco to the Río Salado near the southern nose of the Nacimiento and along the Río Jemez. Using highest/oldest river terraces, resulting bedrock incision values average out glacial/interglacial cycles and are interpreted to reflect differential uplift. For previously mapped and correlated terraces, we applied lidar datasets to refine strath heights. We also utilized new and published dating based on U-series dating of travertine-cemented fluvial deposits, tephrochronology on interbedded ash, and $^{40}Ar/^{39}Ar$ dating of detrital sanidines to constrain terrace ages. Our hypothesis using new geochronology suggests that Quaternary fault slip rates are similar to river incision rates as expected in neotectonically uplifting regions.

TABLE OF CONTENTS

LIST OF FIGURES AND TABLES

Introduction

The Jemez lineament is a NE-trending zone of late Cenozoic (last ~ 6 Ma) dominantly basaltic volcanic fields that have been considered an important tectonic element of northern New Mexico (e.g. Aldrich, 1986; Chapin et al., 2004; Cather et al., 2012) crossing from eastern Arizona (Springerville volcanic field) along a SW-NE trend towards the NE corner of New Mexico (Raton volcanic field), intersecting with the Miocene Río Grande rift in the area of the Valles Caldera (Fig. 1). The southern margin of the lineament is collocated with a lithospheric boundary between the Proterozoic Yavapai (1.8-1.7 Ga) and Mazatzal (1.7-1.6 Ga) Provinces that may have provided a path for magma to ascend to the crust during Cenozoic volcanism (Magnani et al., 2004).

The Jemez lineament has been hypothesized to be a wide zone of dynamic topographic uplift (Formento-Trigilio and Pazzaglia, 1998; Wisniewski and Pazzaglia, 2002; Karlstrom et al., 2012). Recent studies (1-6 of Fig 1 and Table 1) suggest epeirogenic uplift of this wide zone over the past 10 Ma that has driven differential river incision. Cather et al. (2012) identified a broad uplift across the Jemez lineament defined by facies analysis of the Ogallala Formation in the Great Plains. Nereson et al. (2013) identified a NE-trending zone of stream profile convexities and differential incision to support the hypothesis of uplift of the zone relative to the Great Plains with denudation rates of 90-114 m/Ma (Nereson et al., 2013). Repasch et al. (2017) suggested long terms incision rates at Black Mesa and in the Taos Volcanic field of 50-100 m/Ma with variations along the river due to fault-influenced incision rates. Channer et al. (2015) reported

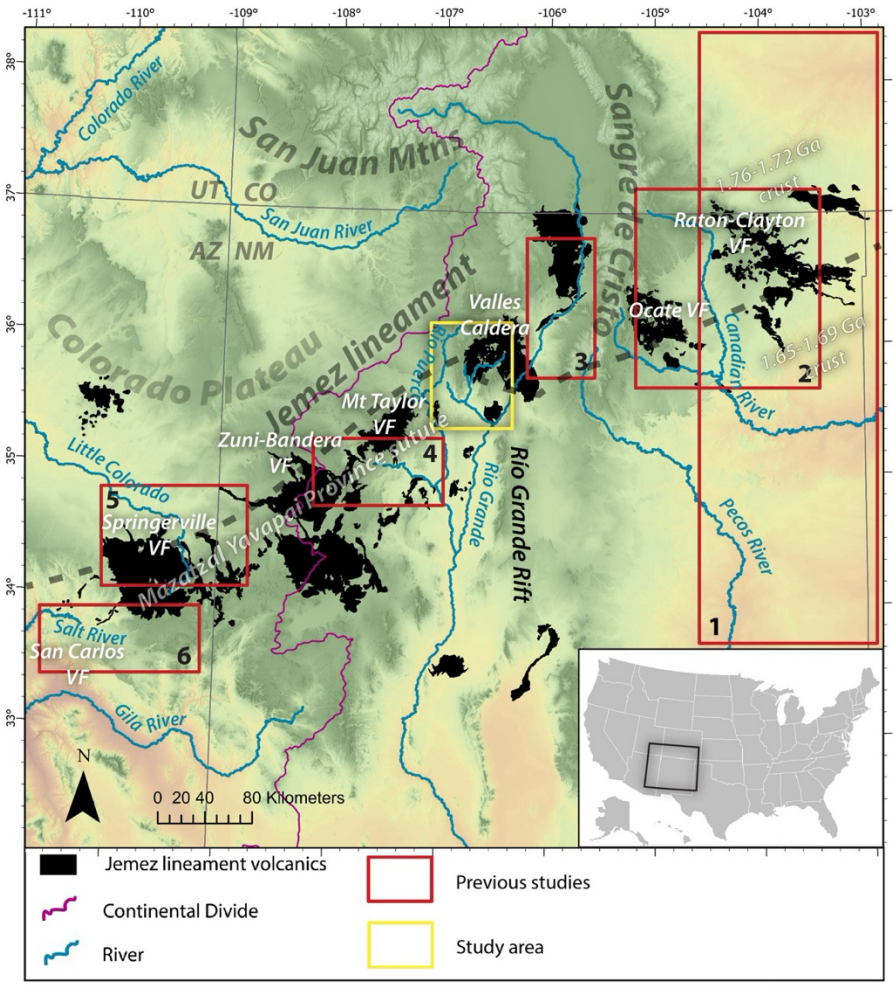

Figure 1: Location of this study (yellow box) and previous studies (red boxes) proposing Quaternary uplift across the Jemez lineament. From NE to SW: 1) Cather et al. (2012), 2) Nereson et al. (2013), 3) Repasch et al. (2017), 4) Channer et al. (2015), 5) Karlstrom et al. (2016), 6) Anderson et al. (2021). The Mazatzal-Yavapai province suture (Shaw and Karlstrom, 1999) is shown collocated with prominent Jemez lineament volcanics and associated NE-trending zone of high topography. This study targets the Valles Caldera area.

incision rates across the Río San José that varied from 19 m/Ma to as much as 288 m/Ma with periods of apparent accelerated incision from 2-4 Ma during construction of Mt. Taylor. Karlstrom et al. (2017) calculated rates of 40-80 m/Ma in the Little Colorado River headwaters and Anderson et al. (2021) reported 95 m/Ma for the headwaters of the Salt River in Arizona.

These variations in rates pose questions about what causes differential river incision along and across the Jemez lineament.

A key area to further test the hypothesis of differential incision and uplift is the Jemez Mountains itself (Fig. 2). This locality features the dynamic interaction of young volcanic systems within the Jemez lineament, Río Grande rift faulting, and bedrock river systems draining high topography. This paper synthesizes and provides new incision rate data for three river

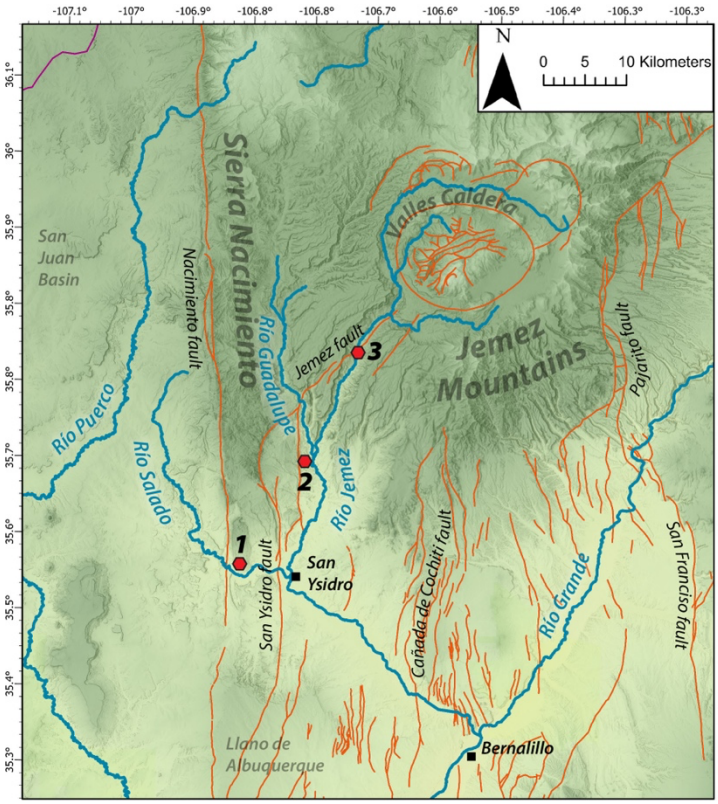

Figure 2: High topography of the Jemez Mountains and Sierra Nacimiento, major rivers, and faults (USGS and NMBMMR, n.d, red lines). Red hexagons indicate the three high terrace localities that form the main topic of this paper: 1) Río Salado terraces on the south plunging nose of the Sierra Nacimiento; 2) Lava Creek B (630 ka) terraces near the confluence of the Río Jemez and Rio Guadalupe; 3) Travertine-cemented gravels on the Río Jemez at Soda Dam.

systems that surround the southwestern side of the Jemez Mountains: Río Jemez, Río Salado, and Río Puerco. We characterize the high topography, examine and compare the river profiles, and

correlate and date river terraces with emphasis on the oldest/highest terraces to derive long-term incision rates.

METHODS

We use diverse methods to measure incision rates, characterize the landscape, and synthesize datasets. Methods used include correlating and dating fluvial terraces in tectonically active terranes (Wegmann and Pazzaglia, 2009; Aslan et al., 2019), tracing detrital sanidine to ignimbrite sources (Heizler et al., 2021), quantitatively analyzing river profiles (Whipple and Tucker, 1999; Wobus et al., 2006; Kirby and Whipple, 2012; Perron and Royden, 2013), parsing Quaternary fault slip by measuring differential incision across faults (Fig. 3; Pederson et al., 2002; Karlstrom et al., 2007; Crow et al., 2014) and testing for potential surface uplift driven by magmatism (Karlstrom et al., 2012).

Geochronology and River Terraces

This study targets mainly strath terraces: the bedrock bench carved by the paleoriver system during periods of incision and capped by a bedload-thickness of gravels and sands. Terrace formation frequently reflects alternating cycles of river incision and aggradation associated with climatic cycles (Love and Connell, 2005; Bridgland and Westaway, 2008). Long-term (> 100s ka) persistent bedrock incision in tectonically active areas can leave stranded terrace flights that record bedrock incision (Fig. 3) that averages out numerous glacial-interglacial cycles and likely records uplift (Karlstrom et al., 2012). Data required for incision rate studies include the height of the terrace strath above the modern bedrock strath (or above river level (ARL) when thickness of gravel is unknown), and the age of the terrace strath (usually a constraining age from the terrace fill). Strath heights were measured accurately using lidar. New and compiled dating relied on various methods with the most robust represented by the

presence of a tephra that was deposited within a terrace fill such as the Yellowstone Lava Creek B ash (LCB, 630 ka; Jicha et al., 2016); these are datable using sanidine $^{40}Ar/^{39}Ar$ dates and/or tephrochronology (both were used in this study). U-series (U/Th) dates on travertine that cement river gravels can provide a direct age (or a minimum age, sometimes difficult to determine) on gravel deposition. Detrital sanidine can be used on "cryptic ashes"—where the presence of an ash component is found as grains worked into deposits without distinct ash layers—and the youngest DS grain provides a maximum depositional age (MDA), that may or may not be close to age of deposition (Heizler et al., 2021).

Modern $^{40}Ar/^{39}Ar$ geochronology methods are derived from K/Ar geochronology methods and are used to date potassium bearing minerals in rocks. The method is based in the natural radioactive decay of ^{40}K ($t_{1/2} \approx 1.25$ Ga) to ^{40}Ar and ^{40}Ca (Schaen et al., 2020) and can be used to date minerals that extend back into Archean. Merrihue and Turner (1966) pioneered the use of ^{39}Ar, derived from ^{39}K during irradiation in a nuclear reactor. Via mass spectrometry, they demonstrated that ^{39}Ar could be accurately measured as a product of ^{39}K. ^{36}Ar is measured to correct for atmospheric ^{40}Ar, allowing a precise measurement of radiogenic ^{40}Ar derived from ^{40}K. Additionally, the production of ^{37}Ar from ^{40}Ca allows for the determination of correction of interfering isotopes of ^{36}Ar and ^{39}Ar that are also derived from Ca. In summary, measurement of radiogenic Ar produced from the decay of ^{40}K ($^{40}Ar^*$) and reactor-derived ^{39}Ar from ^{39}K provides the ability for the $^{40}Ar^*/^{39}Ar_K$ ratio to be used to calculate an age.

Like any geochronologic dating technique, assumptions are made such that the method may provide an accurate age. The first is that $^{39}K/^{40}K$ is near constant in nature, allowing for the measured $^{40}Ar^*/^{39}Ar$ to be proportional to the age of the sample. Other assumptions are that no non-atmospheric ^{40}Ar was incorporated into the sample or that $^{40}Ar^*$ was not lost after

formation, and therefore the system remained closed. During sample dating, a standard sample (flux monitor) of a known age is irradiated with the unknown sample and used to compare with the unknown sample's $^{40}Ar^*/^{39}Ar$. Comparison the flux monitor 40Ar/39Ar with the unknown's 40Ar/39Ar allows for age determination. Because $^{40}Ar/^{39}Ar$ geochronology is based on ratio determinations rather than absolute concentrations of parent and daughter isotopes, very precise age measurements are possible on small samples such single detrital sanidine grains.

$^{40}Ar/^{39}Ar$ dating provides maximum depositional ages (MDAs) for ancestral river deposits. The age of the youngest group of DS grains that have been reworked into a river deposit provides the MDA since the terrace sampled cannot be older than the youngest grain. If calculated MDAs increase systematically with higher and older terraces in sets of terrace flights, the MDAs may be approximate to true depositional ages and can be used to infer rates through time (Aslan et al., 2019). Sanidine grains are collected from samples through sieving for grains ranging from 250-125 microns. These are then washed using distilled water and hydrofluoric acid and undergo heavy liquid separation. Sanidine is distinguished by a lack of microtextures that other feldspars may have under a polarizing binocular microscope. Individual grains are processed for $^{40}Ar/^{39}Ar$ dating via single crystal laser fusion with a CO_2 laser while gases are measured on a ThermoFisher Scientific ARGUS VI multicollector noble gas mass spectrometer at the New Mexico Geochronology Research Laboratory at the New Mexico Bureau of Geology and Mineral Resources in Socorro, NM.

Supplemental to new $^{40}Ar/^{39}Ar$ dates is the extensive legacy U-series geochronology data from travertines within the carbonic systems of the Río Salado and Río Jemez that provide important age constraints on terrace deposition and incision rates through time. Tafoya (2012) and Cron (2011) sampled and dated travertines at Soda Dam and the Tierra Amarilla

anticline/Río Salado terraces, respectively. Both studies drilled and powdered samples that were dissolved in 15N nitric acid and spiked with a solution of know concentrations of ^{229}Th, ^{233}U and ^{236}U. Spiked solutions were dried and redissolved in 7N nitric acid from which they were placed in columns and U and Th were cleaned and separated. After dissolution in nitric acid, separates were analyzed on a Thermo Neptune Multicollector Inductively Coupled Plasma Mass Spectrometer (MC-ICPMS) in the Radiogenic Isotope Laboratory at UNM. Dates obtained by Cron (2011) are from drilled holes in travertine caps. Dates obtained by Tafoya (2012) include a range of samples of micrite, veins, and rinds across the Soda Dam system. Ages reported in this project reflect those calculated by Tafoya (2012) and Cron (2011) including reported model ages for dates beyond the range of U-series dating methods. Model ages help constrain MDA dates for the terraces across the system and have been reprocessed by Victor Polyak.

Terrace flights can yield strath-to-strath ages to test how steady or variable incision rates were through the river's history (Karlstrom et al., 2016; Aslan et al., 2019; Anderson et al., 2021; Crow et al., 2021; Heizler et al., 2021). Rivers cutting across faults may show relationships where a higher rate of bedrock incision in upthrown blocks equals the incision rate on the downthrown block plus the fault slip rate (Howard et al., 1994; Whipple and Tucker, 1999; Tucker and Whipple, 2002; Pederson et al., 2002; Karlstrom et al., 2007; 2008; Whittaker et al., 2008; Crow et al., 2014; Repasch et al., 2017). This method allows for the determination of the magnitude of slip across faults, including those with low-rates on the margins of the Colorado Plateau and Río Grande Rift (e.g. Thompson Jobe and Chupik, 2021).

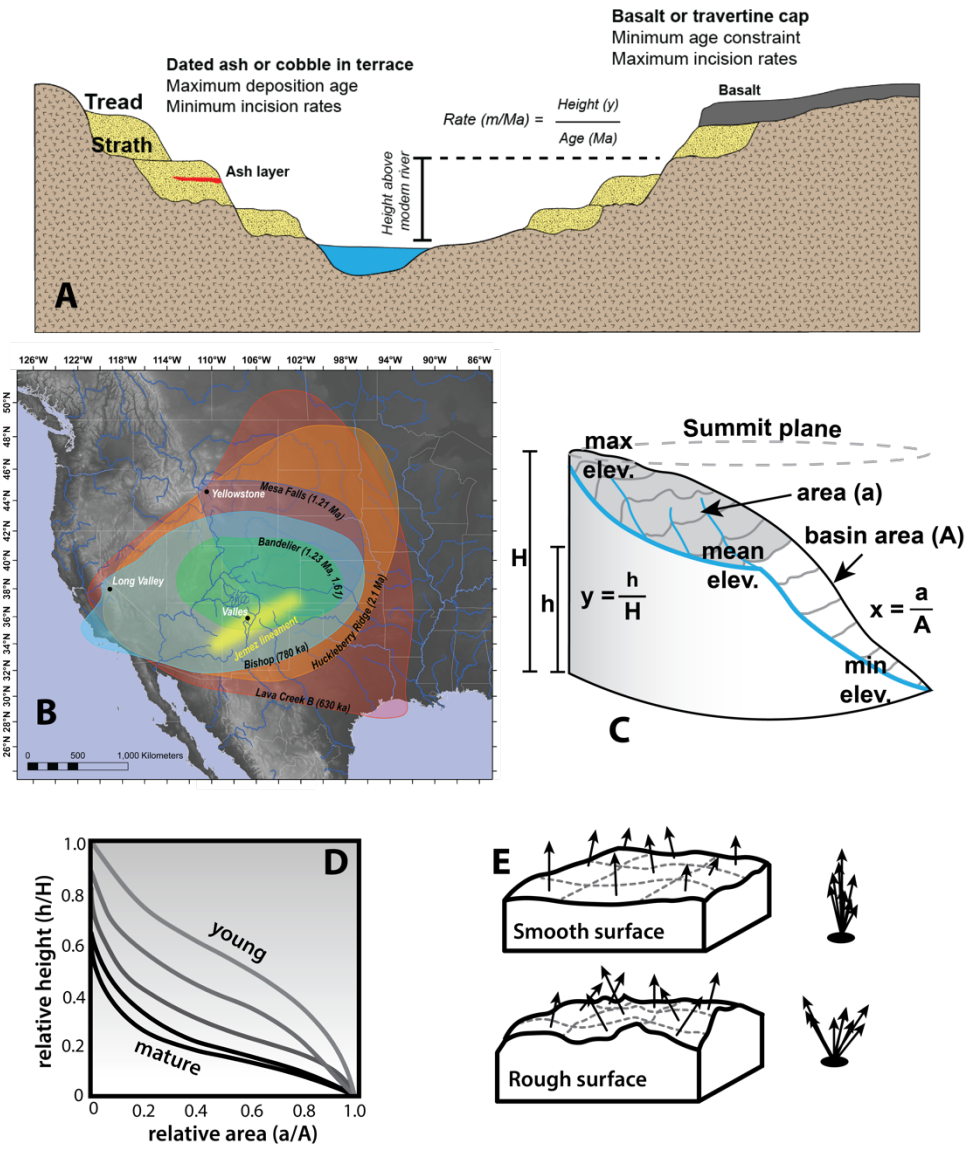

Figure 3. A) Schematic sketch of flight of river terraces. For this study, geomorphic terrace nomenclature and correlation was from Rogers and Smartt (1996), Formento-Trigilio and Pazzaglia (1998), Pazzaglia et al. (1997), Kelley et al. (2023), and was improved using 1m lidar for strath heights above the modern river level (ARL). Using older/higher terraces for incision studies helps average out glacial/interglacial climate cycles to estimate long-term average bedrock incision rates (strath height/age). B) Tephrochronology was used to correlate glass compositions to known Lava Creek B (630 ka) tephra compositions; detrital sanidine analyses were done to constrain maximum depositional age (MDA) and provenance of terrace fills; U-series dates on travertine rinds around and overlying gravels provides a minimum or direct age on gravels. D) Terrain analysis involved hypsometric integral (HI), and E) roughness analysis (Jaiswara et al 2020 after Ohmori 1993) and (Coblentz and Karlstrom 2020, modified).

High Resolution Topographic Data and River Profile Analysis

Quantitative parameters used to investigate erosion of landscapes by bedrock rivers include chi (χ) and k_{sn} steepness indices (Howard 1994, Whipple and Tucker 1999) that may help reveal disequilibrium within the stream driving variable incision rates for example due to knickpoint migration, rock type erodibility differences, or differential uplift. The normalized steepness index (k_{sn}) is quantified using a power law relationship between channel gradient (S) and the upstream drainage area (A) given the reference concavity (θ_n, often 0.45) as shown in Equation 1 (Flint, 1974; Kirby and Whipple, 2012).

$$S = k_s A^{-\theta} \quad (1)$$

When in steady state, the erosion rate of a stream is equal to the rock uplift rate (E=U) and the resulting channel gradient can be described using Equation 2:

$$S_e = \left(\frac{U}{K}\right)^{1/n} A^{-m/n} \quad (2)$$

whereby K is the erosional efficiency factor that accounts for lithology, climate, channel geometry, and sediment supply (Howard et al., 1994; Whipple and Tucker, 1999), and the m/n ratio represents stream power per unit area or other channel dynamics (Tucker and Whipple, 2002). χ (Chi) is the inverse integral of the drainage area (Perron and Royden, 2013):

$$\chi = \int_{\chi_b}^{\chi} \left(\frac{A_0}{A(\chi)}\right)^{-\theta_n} dx \quad (3)$$

where A_0 is the reference drainage area. χ analysis of the Río Salado and Río Puerco basins provides information to determine any significant transient Quaternary or future disturbance along divide of the basins. χ disequilibria across basin divides suggests preferential migration of the divide from lower to higher χ values unless maintained by differences in lithology or uplift (Willett et al., 2014). χ analysis of the Río Salado and Río Puerco basins will provide information to determine any significant transient Quaternary disturbance along divides of the

basins and will help identify if the Rio Jemez-Río Salado system is in equilibrium or actively adjusting, for example to bedrock variations, geomorphic forcings like stream capture, or tectonic forcings like differential uplift.

Morphometric tools to evaluate landscape maturity and evolution include the hypsometric integral (HI) and roughness. Hypsometric integral is the area below the hypsometric curve (Fig. 3D) representing the area below a relative elevation (Strahler, 1952). In Fig. 3D, H is the relief in the basin and total surface area of the basin is represented by A while area (a) is the surface area above a given elevation (h). Landscapes that have reached maturity generally have lower HI and concave curves while youthful landscapes have higher HI and convex curves (Strahler, 1952). By plotting the HI value of a moving window, it is easier to visualize areas of young relief versus areas of preserved eroded surfaces. Roughness, or the ruggedness index, quantifies the mean absolute difference in elevation from one cell to the next (Fig. 3E) and can clearly display young geomorphic features like scarps and offsets better than a traditional hillshade model.

TopoToolbox, a Matlab-based plug-in software for geomorphic modeling (Schwanghart and Scherler, 2014), was used to conduct these analyses. A 1m lidar-derived DEM of the study region was resampled to a 5m resolution to allow more efficient processing with robust result for k_{sn} analysis (Purinton and Bookhagen, 2017). Analysis of roughness and hypsometric integral (HI) was completed using TopoToolbox with a 2000 cell moving window. χ analysis was done using ChiProfiler (Gallen and Wegmann, 2017) that utilizes TopoToolbox in the Matlab environment.

RESULTS

Terrain Analysis

Figure 4A shows the hypsometric integral from the elevation-relief ratio (per Pike and Wilson, 1971) processed for the landscape around the Jemez Mountains and Sierra Nacimeinto from a 10m DEM. This evaluates the relative development stage of topography (Strahler, 1952; Ohmori, 1993; and Jaiswara et al., 2020). Low values are representative of extensive level surface with isolated relief features, like floodplains, whereas high values can be reflective of broad level surface broken by depressions or incised features (Pike and Wilson, 1971; Fig. 4A). The elevation-relief ratio of the area surrounding the Jemez Mountains and the Sierra Nacimiento may demonstrate the relative youthfulness of the high topography in contrast to the well-adjusted and incised front of the Sierra Nacimiento and Río Jemez floodplain. The Sierra Nacimiento and Jemez Mountains in this view are difficult to decouple and have similar N-S dimensions of high and incised topography, raising the possibility that both are responding to the Quaternary landscape perturbation caused by surface uplift of the Jemez Mountains due to volcano construction plus potential epeirogenic uplift.

In roughness (Fig. 4B), the Jemez Mountains and Sierra Nacimiento are both rugged landscapes relative to the San Juan Basin to the west and the Río Grande rift to the southeast. The roughness map (Fig. 4B) is similar to Fig. 4A in highlighting major tectonic features, such as the 80–km-long Sierra Nacimiento uplift bounded by the Nacimiento fault zone and the closely corresponding elevation, diameter, and roughness between the Sierra Nacimiento and Jemez Mountains. Incised features such as Cañon de San Diego (CdSD on Fig. 5) are clear in both images, reflecting rapid Quaternary incision that is leaving high topography stranded.

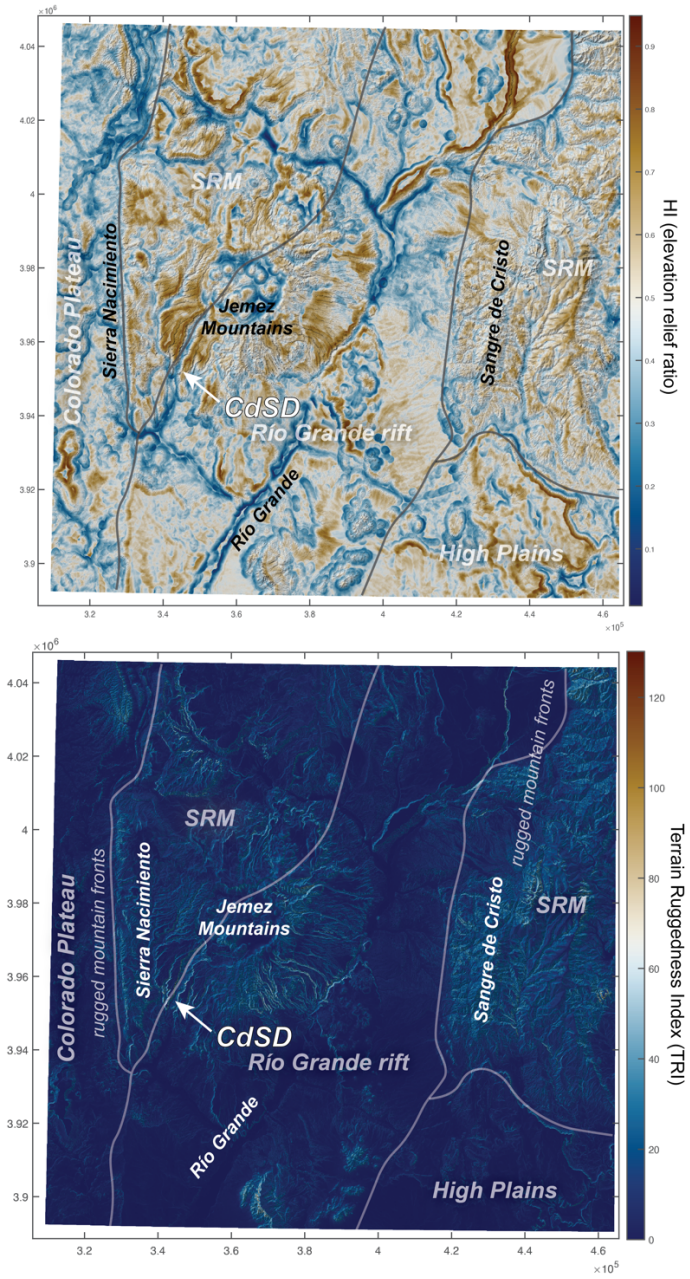

Figure 4: Terrain analysis. A) Hypsometric integral (HI) map, calculated using the elevation-relief ratio method of Pike and Wilson (1971), shows the extent of broad high topography incised by narrow canyons in the combined Jemez-Nacimiento uplifts. The Jemez-Nacimiento uplift hypsometry is filtered through a 200 cell (10m) radius moving window and is consistent with relative youthfulness of the uplifts. However, extensive areas of high values in the Jemez Mountains spatially correspond to the 1.2 Ma Bandelier Tuff or relatively young basalt flows, which obscures conclusions of tectonic uplift versus young topography due to a thick ignimbrite. B) Roughness map shows high roughness in what we interpret to be neotectonically uplifting topography. The similar dimensions and geomorphic states of the Quaternary Jemez Mountains and the Laramide Sierra Nacimiento suggests the possibility that Quaternary and ongoing uplift of the Jemez Mountains is driving renewed uplift of the southern Sierra Nacimiento. Elevated roughness gradients in the Sangre de Cristo clearly trend across mountain front faults and harder lithologies.

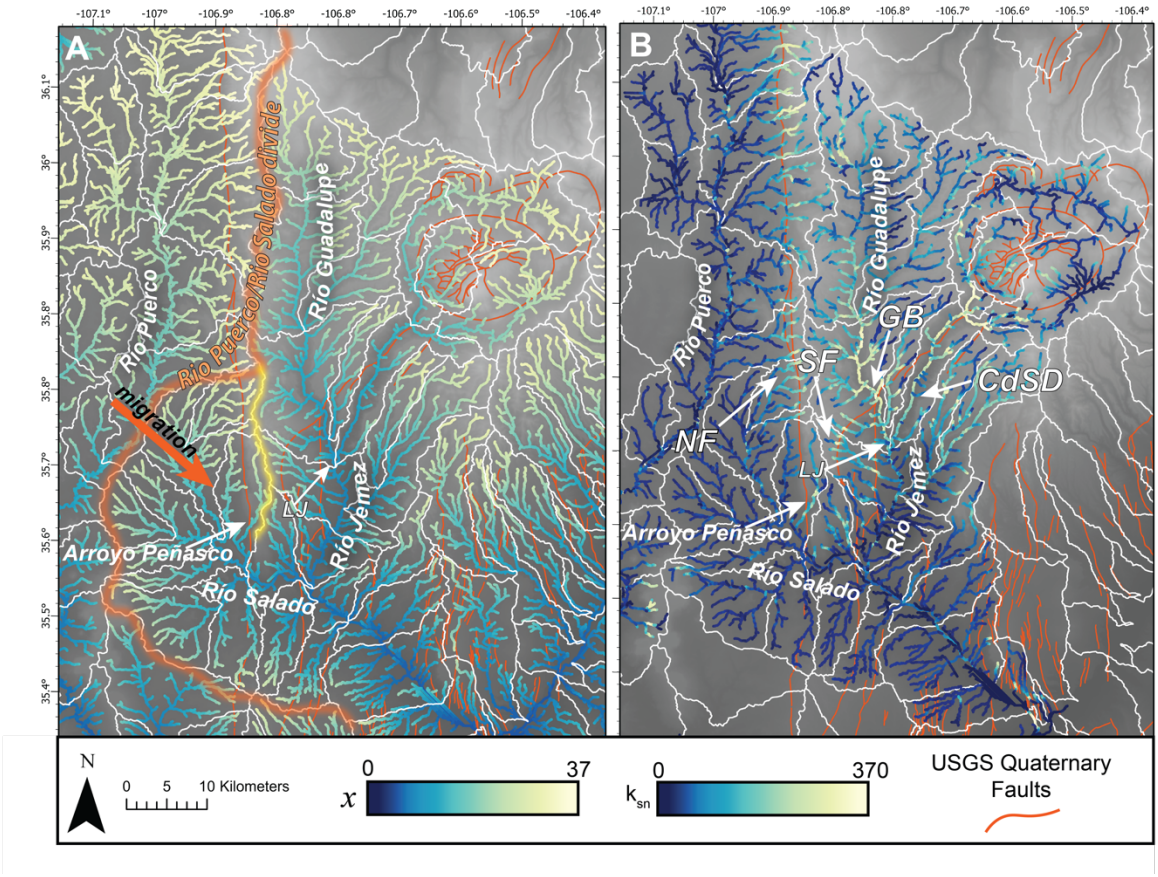

Figure 5: A) χ analysis shows divide instabilities between the Río Puerco and Río Salado, with higher χ in the Río Salado than the Río Puerco that favors divide migration into the Río Salado drainage. B) k_{sn} analysis of normalized river steepness from 10m and 5m DEM respectively shows over-steepened reaches in the Precambrian basement of the Sierra Nacimiento and Nacimiento fault (NF), in the Río Jemez of Cañon de San Diego (CdSD), in the Río Guadalupe and Guadalupe box (GB), and across some faults. Basin divides are shown in white (USGS, 2019). The confluence of the Río Guadalupe with the Río Jemez, La Junta, is labeled LJ. Quaternary faults are shown in red (USGS and NMBMMR, accessed 2024).

χ values (Fig. 5A) and k_{sn} (Fig. 5B) of the Río Jemez basin and adjacent rivers show over-steepened reaches caused by lithologic and tectonic controls. χ, a measure of basin divide stability, can assess basin-level rather than stream-level disequilibrium (Willett et al., 2014). χ analysis (Fig. 5A) reveals significant disequilibrium across two divides: the Río Puerco/Río Salado and the Arroyo Peñasco/Río Salado divides. The Arroyo Peñasco-Río Salado basin has

higher χ than neighboring basins, suggesting that lithology and/or tectonic controls are maintaining high χ values across the southern nose of the Sierra Nacimiento. This analysis may also reflect the capture of the Arroyo Peñasco by the Río Salado that was interpreted to be due to erosional variability of lithology (Formento-Trigilio and Pazzaglia, 1998) compatible with a young, disequilibrium, river system responding to lithologic and tectonic controls.

Within the k_{sn} map, steeper normalized channel gradients are collocated with major faults and lithologic changes (Fig. 5B, 6). The relatively low k_{sn} of the Río Guadalupe and Río Jemez at La Junta (LJ of Fig. 5B) supports that the two rivers are currently at a state of relative equilibrium (Rogers, 1996). Notable areas with elevated k_{sn} include reaches of the Río Guadalupe (e.g., GB is the Guadalupe box in Fig. 5B) and the Río Jemez upstream from La Junta (Fig. 5B). Additionally, tributary streams that cross the San Ysidro-Jemez fault zone have higher k_{sn} on the upthrown side of the fault. Some faults exposed resistant basement rocks leading to over-steepened reaches making it difficult to parse lithologic versus tectonic controls, like across the Nacimiento front and Guadalupe box (GB and NF of Fig. 5B) where lithology likely contributes to steepness. Other areas of high k_{sn} primarily reflect faults and fault-related knickpoints such as the over steepened reaches draining the southeastern Sierra Nacimiento as demonstrated in Fig. 6.

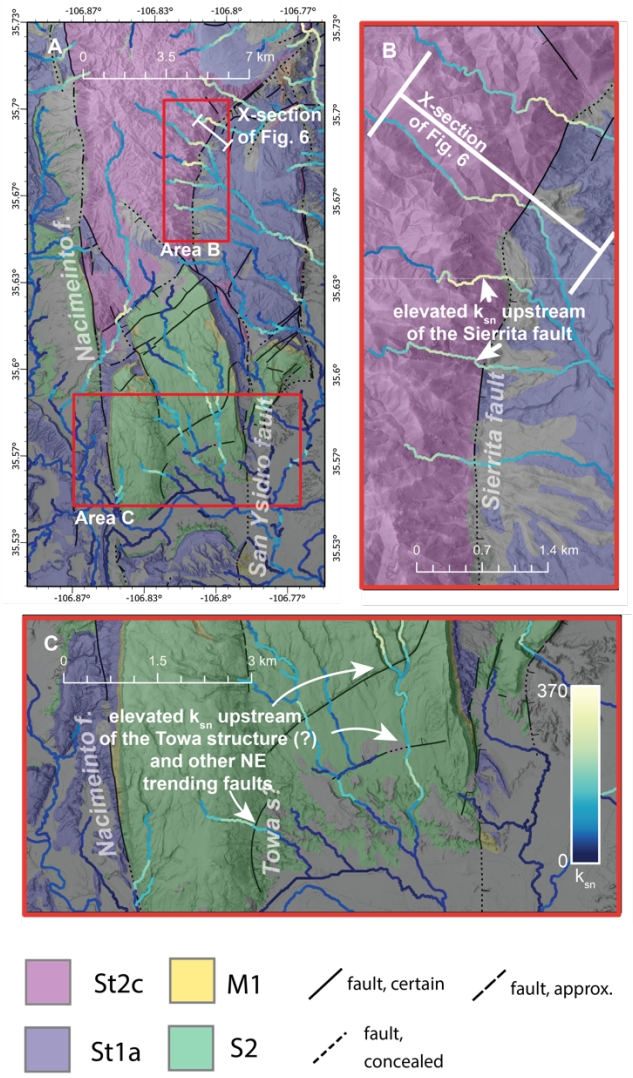

Figure 6: Detailed k_{sn} maps of tributary drainages in the southern Sierra Nacimiento. (A) Index for large scale maps of eastern slope of the southern Sierra Nacimiento (B) and the southernmost Sierra Nacimiento (C). Note that the stream color shades relate to k_{sn} (as shown in C) and the map-area shades correspond to lithology (key at bottom of figure). Map colors correspond to estimated rock hardness from Cikoski and Koning (2017), helping estimate relative stream response to both lithology and tectonics. In increasing magnitude of hardness, the units are categorized as: S2 (green, weak sedimentary rocks that are well consolidated and mostly cemented), M1 (yellow, interbedded weak and strong sedimentary rocks, assumed moderate strength), St1a (indigo, hard caprock underlain by softer sedimentary rocks), St2c (pink, thick Proterozoic rocks). We use an informal term, the Towa structure, to tentatively link: 1) partially reactivated E-up monocline S of Highway 550 also mapped by Kelley (), linear E-down ramp in Agua Zarca- Petrified Forest contact that hosts travertine-depositing springs, and potential linkages to E-down and SE-down faults mapped by Woodward and Ruetschillang (1976) and Kelley (1977). The tributaries of the Río Salado cross the Towa structure and other NE-trending structures with normal displacement. The Towa is down to the SE as is another NE trending fault, and both show tributaries with high steepness at and upstream of the fault. B) Tributaries crossing the Sierrita (down to the east) also exhibit steeper reaches at and upstream (west) of the fault with section of Figure 6A block diagram shown. Local context near the Río Salado (C) shows tributary channels exhibiting the same response to faults.

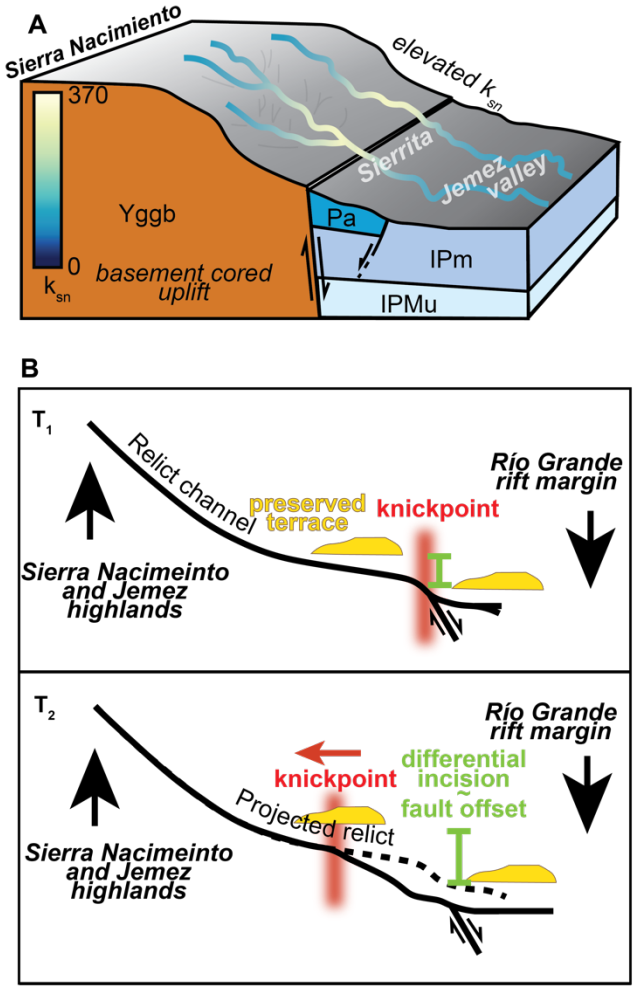

Figure 7: A) Simplified block diagram with the basement cored uplift of the Sierra Nacimiento and the normal Sierrita fault. Tributary streams have steeper reaches at and just upstream of the fault (high k_{sn} values that may correspond to knickpoints) but upstream return to concave-up (equilibrium) profiles (low k_{sn} values). B). Time series diagrams of stream profiles provide an explanation for observed steepness knickpoints collocated at faults as transient responses to fault movement and base-level fall/headwater uplift. The knickpoint propagates upstream as the channel responds to the change. The offset can be measured by offset on preserved terraces, primarily on mainstem streams. Time series adapted from Armstrong et al. (2021).

Examination of the k_{sn} analysis of tributary streams in the southern Sierra Nacimiento (Figure 6A) reveals that elevated k_{sn} values are concentrated upstream of major fault segments suggesting a response to young movement across the faults. Two regions of interest are where tributary streams cross normal faults. Rock strength and hardness are classified by color

according to Cikoski and Koning (2017) to account for generalized lithologic influences on steepness. Figure 6B shows tributaries draining the eastern slopes of the Sierra Nacimiento to the Río Jemez and crossing the Sierrita fault and a N-trending segment of the San Ysidro-Jemez fault system. These show elevated k_{sn} upstream of multiple faults then a return to near equilibrium gradient farther upstream – all in the same generalized map unit. Figure 6C shows streams that cross an informally named Towa structure that show similar pattern across multiple faults all within the Penn-Permian section of uniform hardness that only in part reflects contrast between basal Agua Zarca Sandstone and weaker Petrified Forest Formation. These patterns suggest neotectonic movement across faults as a primary control on these tributary gradients that is enhanced when Precambrian bedrock is brought up on the faults such as at Sierrita fault of Fig. 6B.

The observed steepened reaches and knickpoints of tributary streams (high k_{sn}) support evidence of a neotectonically active landscape in the southern Sierra Nacimiento across major fault segments. Figure 7A demonstrates a conceptualized block diagram of tributary streams crossing a normal fault (like the Sierrita) with k_{sn} patterns shown as the color gradient. Where the normal fault brings up harder basement rock in the footwall, this contributes an additional lithologic control that is superimposed on knickpoint formation (Wobus et al., 2006). Figure 7B shows a time series as the knickpoint widens and migrates upstream. Terraces are offset and differential heights relative to the steepened profile reflect fault slip. Thus, for the Sierrita fault and the ENE striking faults on the southeastern end of the Nacimiento Mountains, we interpret k_{sn} data to indicate tributaries that are adjusting to Quaternary faulting.

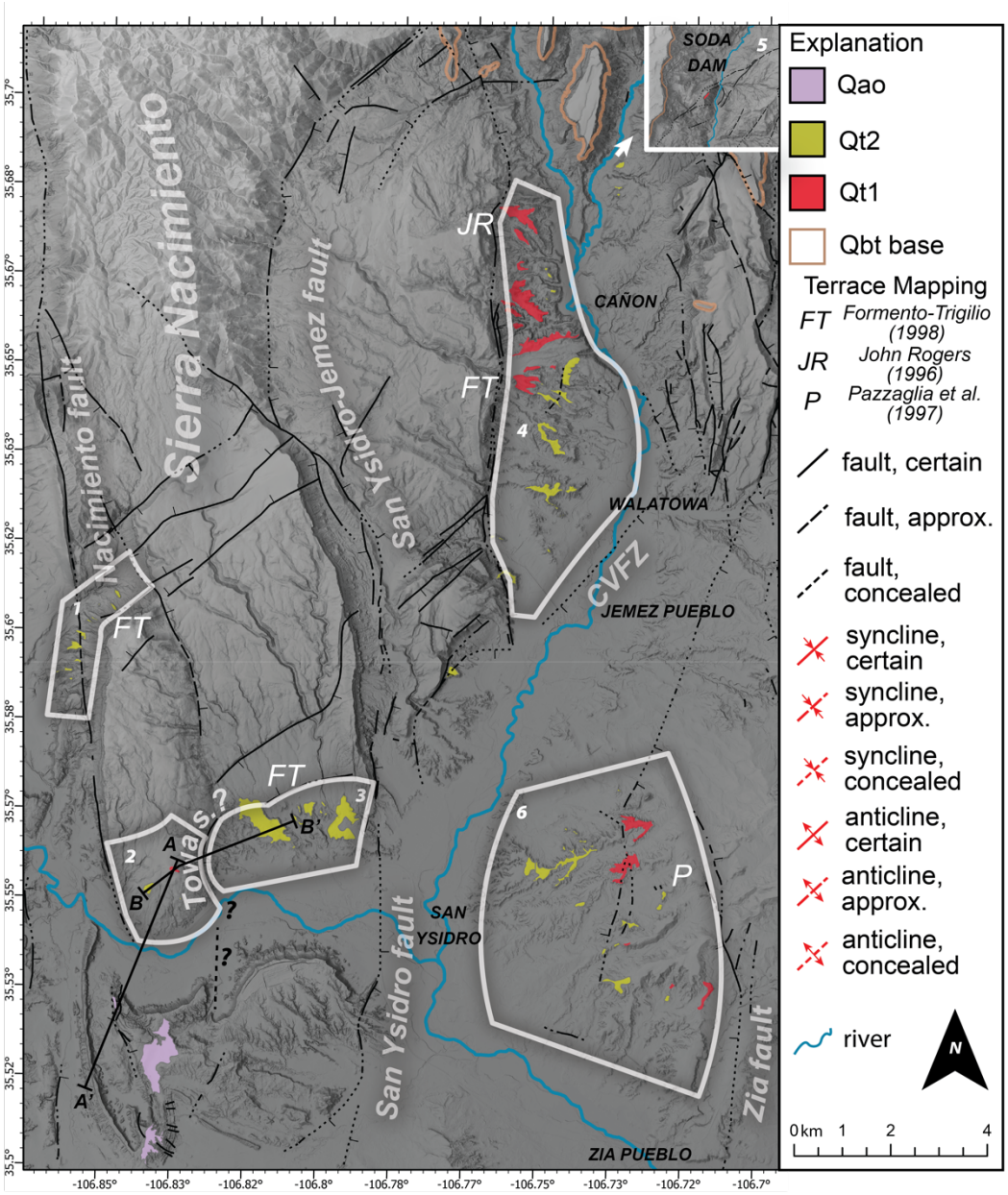

Figure 8: Six areas where terrace flights are correlated by height, age, and fill/tread/soil character are shown. Qao is defined as Quaternary aeolian + alluvial deposits that cap the beveled surfaces across the Tierra Amarilla anticline, Qt2 is the second highest terrace correlated across the Río Salado and Río Jemez (Formento-Trigilio and Pazzaglia, 1998; Formento-Trigilio et al., 1998; and Kelley et al., 2023), Qt1 is the highest correlated terrace of the Río Salado and Río Jemez system (Formento-Trigilio and Pazzaglia, 1998; Formento-Trigilio et al., 1998) and Kelley et al., 2023). Subareas are:1) **Arroyo Peñasco**: terraces commonly overlain by travertine-cemented platforms. 2) **Rio Salado**: the nose of the Sierra Nacimiento has gravel terraces cemented by travertine, which was dated using U-series methods. 3) **San Ysidro**: Río Salado terraces located 2-4 km west of San Ysidro. 4) **Walatowa** (south) and **La Junta** (north): Río Jemez terraces at Walatowa and La Junta near the Jemez-Guadalupe confluence include a Lava Creek B (630 ka) ash-containing terrace (Qt1). 5) **Soda Dam:** U-series dated travertine-cemented gravels at Soda Dam on a structural horst within the Jemez fault zone. 6) **Zia Pueblo:** Located 1-6 km east of San Ysidro, these terraces may contain past paleoconfluence locations of Río Salado and Río Jemez.

	Terrace Group	Heights ARL (m)	Ages (ka)	Incision Rates (m/Ma)	Fault	Est. slip (m) (terrace used)
1	Arroyo Peñasco	Qt2: 80m	none* Qt2: 415[1]	193*		
					Nacimiento fault	<50 (Qt2)
2	Río Salado	Qt1: 164 m Qt2: 130 m Qt4: 44 m	Qt1: 534 ± 148 [2] Qt2: 415 ± 16 [3] Qt4: 259 ± 3 [4]	Qt1: 307 Qt2: 313 Qt4: 170		
					Towa structure	<85 (Qt2) ~0 (Qt4)
3	San Ysidro	Qt2: 45m Qt4: 45m	Qt2: 400 ± 100 [5] Qt4: 259 ± 3 [4]	Qt2: 113 Qt4: 174		
					San Ysidro + CVFZ	25 (Qt2)
4	Walatowa	Qt1: 110m Qt2: 70m Qt4: 30m	Qt1: 631 ± 1 [6] Qt2: 415 ± 16 - 500 [7]	Qt1: 174 Qt2: 169		15 (Qt4)
	La Junta	Qt1: 90m Qt2: 70m Qg3: 185m	Qg3: 1.23 Ma [8]	Qt1: 143 Qt2: 169 Qg3: 150		
					Jemez fault	60 (Qt1)
5	Soda Dam	Qt1: 150m Qbt: 385m	Qt1: 486 ± 125 [9] Qbt: 1.62 Ma [10]	Qt1: 309 Qbt: 238		

60 m
85 m
25 m

3	San Ysidro	Qt2: 45m Qt4: 45m	Qt2: 400 ± 100 [5] Qt4: 259 ± 3 [4]	Qt2: 113 Qt4: 174		
					San Ysidro fault	15 (Qt2) 11 (Qt4)
6	Zia	Qt1: 100 m Qt2: 60-65m Qt4: 34 m	Qt1: 631 ± 1 [11] Qt2: 400 ± 100 [12] Qt4: 259 ± 3 [5]	Qt1: 160 Qt2: 150 Qt4: 130		

River Terrace Correlations

Figure 7 shows our river terrace correlations along the Río Salado-Río Jemez system. The Río Salado drains the western Sierra Nacimiento and joins the Río Jemez that drains the Jemez Mountains to form a major tributary to the Rio Grande. Because of the numerous faults that cross the rivers, we divide the terraces into fault-bounded subareas, within which flights of terraces have not been significantly modified by faulting (subareas 1-6 of Fig. 8). These terraces have

been traced and correlated by several workers within these areas (e.g., Rogers, 1996; Rogers and Smartt, 1996) and between a these areas (Formento-Trigilio and Pazzaglia, 1998; Tafoya, 201;

Figure 9 (previous page): Summary table and index map of terrace ages, heights, and incision rates for each terrace subarea (1-6) with differences in incision rates between subareas attributed to post-630 ka fault slip on the fault segments shown. Arrows on faults indicate relative movement (E or W side down) as if in cross sectional view from the south. Longer term bedrock incision (canyon deepening) rates are shown from the base of the lower Bandelier where available (see text for complexities). Differential incision is calculated between available correlated terraces, either Qt2 or Qt1 and assumes the high terraces at Soda Dam and Sierra Nacimiento may correlate to the 630 ka Lava Creek B terrace, which is permitted but not dictated by the data. Footnotes (superscript numerals in Ages column) are as follows:

1. Formento-Trigilio and Pazzaglia (1998) correlate these surfaces that locally interfinger with Qt2 with other Qt2 terraces on the Río Jemez. Qt2 is determined to be >415 ± 16 ka based on a 415 ± 16 ka U-series age from the Río Salado flight and is within range of proposed ages for Qt2 from Rogers (1996) of 310 ± 70 ka to 425 ka and Formento-Trigilio and Pazzaglia (1998) of 400 ±100 ka.
2. U-series model age on travertine caps on highest terraces from Cron (2012). The high Qt1 terrace on the Río Salado is estimated at 630 ka since it is beyond U-series dating range, the next lower sets are >415 ± 16 ka, and the highest terrace across this system.
3. U-series age on travertine caps on second highest terraces from Cron (2012).
4. Age estimate from Formento-Trigilio and Pazzaglia (1998) based on soil profiles of correlated terraces along the Río Jemez.
5. Age estimate from soil profiles from Formento-Trigilio and Pazzaglia (1998) for terraces near Walatowa and correlated with nearby age of 259 ± 3 ka for 44m terrace in subarea 2.
6. Age from determination of presence of LCB ash (Rogers, 1996; Pazzaglia et al., 1997; this study). All other Qt1 terraces are correlated to the dated LCB (630 ka) ash layer within the Qt1 terrace at La Junta confirmed by $^{40}Ar/^{39}Ar$ detrital sanidine geochronology and tephrochronology.
7. Age estimates for Qt2 from Cron (2012) and Rogers (1996).
8. Nasholds and Zimmerer (2022) age of Tshirege member of the Bandelier Tuff refining the age of Qg3 determined by Rogers (1996).
9. Minimum age from Cron (2012) U-series model age on calcite vein in gravels.
10. Nasholds and Zimmerer (2022) age of Otowi member of the Bandelier Tuff.
11. Age estimate of Qt1 from Pazzaglia et al. (1997).
12. Age estimate from soil profiles taken near Walatowa for Qt2 terraces by Formento-Trigilio and Pazzaglia (1998).

* No age constraints available, see Formento-Trigilio and Pazzaglia (1998).

Kelley et al., 2023) but ours is the first attempt to integrate all six areas including the newly dated terrace flight on the southern nose of the Sierra Nacimiento. The terrace flight subareas include the southwest flank of the Sierra Nacimiento (subarea 1), the south-plunging nose of the

Nacimiento uplift (subarea 2), the Salado-Jemez confluence near San Ysidro (subarea 3), the lower Río Jemez (subarea 4), Soda Dam area (subarea 5), and near Zia Pueblo (subarea 6). Formento-Trigilio and Pazzaglia (1998) correlated terraces across subareas 1, 3, 4, 5, and 6, but we add new geochronology and refined heights from 1m lidar. Rogers and Smart (1996) and Rogers (1996) worked in subarea 4 and calibrated long-term rates with a key terrace that contains the Lava Creek B ash (630 ka). For subareas 2 and 5 we present new terrace characterization and U-series and DS geochronology. These data significantly change the terrace correlation of Frankel and Pazzaglia between subareas 4 and 5 (2006, their Fig. 8).

Terrace Heights and Ages

Figures 8 and 9 summarize height and age information for key terraces from each subarea. These refined heights and ages can be used to test the correlation of Formento-Trigilio and Pazzaglia (1998), essentially followed by Kelley et al. (2023), who named and correlated Qt1 and Qt2, the highest and second highest mapped Quaternary terraces within each flight, as well as lower terraces Qt3 to Qt6 leading down to the active flood plain. Formento-Trigilio and Pazzaglia (1998) proposed a fault-influenced incision model and identified several Quaternary faults based on terrace offsets. The next section of the paper tests this correlation with focus on the higher terraces in subareas 2, 4, and 5 where our geochronology data shows lower incision rates in subarea 4 than in subareas 2 and 5 over the past ~ 500 ka. The published correlations combined with our preferred ages for subarea 5 would necessitate large offset across the Towa structure. We also explore alternative terrace correlations that partition this differential incision across other faults.

A terrace flight at Río Salado (subarea 2) on the S-plunging nose of the Sierra Nacimiento is newly described and dated in this paper and provides a potential template for

terrace correlation. Eight thin (few-m-thick) terraces of river cobbles and sands rest on a thin skin of Petrified Forest Member of the Chinle Formation preserved on the Agua Zarca dip slope and many are capped by travertines (Fig. 10). Although U-series ages of travertine are minimum ages, we assume that travertine deposition closely followed strath and floodplain development, perhaps within several to 10 ka and within the error of the U-series dates. This assumption is based on the semi-regular ~100-ka-scale of increasing age upwards in the terrace flight, the analogy to the modern river where modern ojitos are depositing travertine mounds atop Río Salado alluvium in the modern floodplain, and the apparent role of travertine deposits in preserving both the thin skin of Petrified Forest Member and the thin gravels on the Agua Zarca dip slope. U/Th dates on samples of travertines capping Río Salado gravels are shown in Figure 10A and listed in Table 1. The highest terraces (Qt1a and 1b) are 195m and 164 m ARL and ages are beyond U-Series range (> 500 ka), but Qt1b gives a ^{238}U model age of 534 ± 148 ka. We tentatively correlate Qt1 to here based on relative height differences of Qt1 and Qt2 elsewhere (~20-40 m; Fig. 9), which is allowable by the Qt1b model age. The next highest terrace (Qt2) is 130m ARL and gives a U-series date of 415 ± 16 ka. Qt4 is 44 m ARL and gives a U-series age of 250 ka. $^{40}Ar/^{39}Ar$ DS samples were collected from terrace fill beneath several of the dated travertines with youngest grains of ~1.2 Ma; these provide maximum age constraints that are compatible with the U-Series dates, but do not further help refine the strath ages (Table 1).

Subarea 3 (Fig. 9) is on the Rio Salado and contains the San Ysidro terraces. Formento-Trigilio (1997), Formento-Trigilio et al. (1998), and Formento-Trigilio and Pazzaglia (1998) correlated Qt2 (55 m) in this area to the Qt2 (45m) in subarea 4 where they estimated an age of 400 ± 100 ka based on soil development. This age is similar to the 415 ± 16 ka U-series dated travertine of Qt2 (130 m) in subarea 2. If this published correlation is correct (our Alternative 1),

there is a 75m height difference of the ~400 ka terraces between subareas 2 and 3 that could be explained by 75m of E-down displacement across the Towa structure in the past 400 ka. The base of the Petrified Forest Formation is an E-down ramp or monocline with about 100m of vertical separation, but there is no obvious fault plane or scarp. An alternative correlation (Alternative 2) would be to correlate Qt2 and Qt4 in subarea 3 with the 250 ka Qt4 in subarea 2. In this alternative correlation, there need be no Quaternary displacement across the Towa structure but it allows offset on the San Ysidro fault.

Subarea 4 is on the Río Jemez and extends from Walatowa to the Río Jemez-Río Guadalupe confluence at La Junta. It has a well-developed terrace flight on the west side of the river, and less well preserved paired terraces on the east. The highest terraces at La Junta (Fig. 11) are an important keystone that provides an age for Qt1 because it has the 630 ka (Jicha et al., 2016) Lava Creek B (LCB) Yellowstone ash in it (Rogers, 1996; Rogers and Smartt, 1996). The Qt1 terrace (Fig. 11A) is a fill terrace that sits upon a well-preserved strath developed on Permian sediments (Abo Formation) and consists of 22 m of sediment (~3-4 m of cemented river cobbles with sparse fine sand lenses overlain by 11 m of sands, silts, and fine gravels overlain by 7 m of coarse gravel; Rogers and Smartt, 1996, Fig. 5). A prominent 1-2m thick ash-rich layer sits 5m above the strath and is capped by about 17m more alluvium and terrace deposits.

We resampled the terrace and ash in several places for $^{40}Ar/^{39}Ar$ dating to confirm the presence of 630 ka Lava Creek B ash. We sampled at the strath within a sand lens (CR22-G1), the basal part of the ash layer (CR22-G2), and the terrace material above the ash layer (CR22-G3). $^{40}Ar/^{39}Ar$ dating (Fig. 11B) for all three samples returned bimodal weighted MDAs with a prominent peak at 1.22 Ma (Upper Bandelier Tuff, UBT) and one centered at 604 ± 15 ka, the latter comprised exclusively of grains from sample CR22-G2 (the ash sample). The oldest

normal distribution of the youngest grains provided a date of 633 ± 10 ka (Fig. 11B). The older age closely matches the known age of the LCB eruption (630 ka, Jicha et al., 2016) compared to the youngest normal distribution of 533 ± 16 ka which may be explained by ^{40}Ar loss. We also processed volcanic glass samples for microprobe tephrochronology to determine agreement with the microprobe analysis of Rogers (1996) given the alternate possibility that such a well preserved ash may be from the nearby Valles caldera. Results confirmed a match in tephra chemistry (CaO vs.FeO) of the CR22-G2 sample (Fig. 11C black dots) with that of LCB (red circles; Perkins et al., 1995) and not with the Tshirege Member of the Bandelier Tuff or ash-fall units of the Pajarito plateau (Woldegabriel et al., 2007). Our results agree with Rogers (1996) and provide additional geochronology for this ash. Using a strath height of 90m for Qt1 in subarea 4, we calculate an average bedrock incision rate of 143 m/Ma since 0.63 Ma. Rogers (1996) cited an incision rate of ~150 m/Ma using the tread height of 111 m (rather than the 90 m strath height) and an LCB age of 620 ka (rather than 630 ka).

For Qt2 in subarea 4, Rogers (1996) estimated an age of 500 ka using a combination of stratigraphic position, amino acid racemization ratios, incision rates, correlation with dated terraces of the Río Chama, and an attempt to correlate terrace formation with the glacial and interglacial oscillations calibrated by the marine isotope stage (MIS) curve. This estimated age is approximately compatible with our 415 ka age from subarea 2.

Figure 10 shows Qt1 in subarea 2 as 164 m ARL, 534 ka, yielding an incision rate of 307 m/Ma; and Qt2 as 130m ARL, 415ka, yielding an incision rate of 313 m/Ma. Near La Junta area (subarea 4), the Qt1 strath is 90 m ARL and we use the Lava Creek B ash age of 630 ka, yielding a lower incision rate of 143 m/Ma. This rate is consistent with the incision rate of 175 m/Ma for Qt2 using 70 m ARL and 400 ka. The difference in incision rates between subarea 2 (~ 310

m/Ma) and subarea 4 (~ 140 m/Ma) is 170 m/Ma, hence 85 m over the past 500 ka. The height difference of 74 m for Qt1 and 60 m for Qt2 for age-correlative terraces between subareas 2 and 4 is attributed to differential incision due to faulting. With Alternative 1, correlating terraces between subareas 2 and 3 result in 74 m of vertical displacement across the Towa structure. The Alternative 2 correlation between the two subareas (i.e., correlate Qt2 and Qt4 in subarea 3 with the 250 ka Qt4 in subarea 2), results in zero displacement across the Towa structure and up to 60-70 m of vertical displacement on the Jemez-San Ysidro fault (the 60-70 m is obtained from comparison of the Qt1 and Qt2 heights in subareas 4 and 6, east of the fault, with Qt1 and Qt2 heights in subarea 3, west of the fault). The resulting vertical offset value (60-70 m) value is higher than the 6-11 m of post-630 ka vertical offset interpreted on the San Ysidro fault by Formento-Trigilio and Pazzaglia (1996) and Formento-Trigilio (1997). The calculated slip rate for using the alternative correlation results in a vertical slip rate of ~100 m/Ma, which is compatible with a Late Quaternary slip rate of <200 m/Ma for the San Ysidro fault (Kelson et al., 2015) and higher than the 27-54 m/Ma interpreted for its southern extension, the Calabacillas fault (McCalpin, 2011).

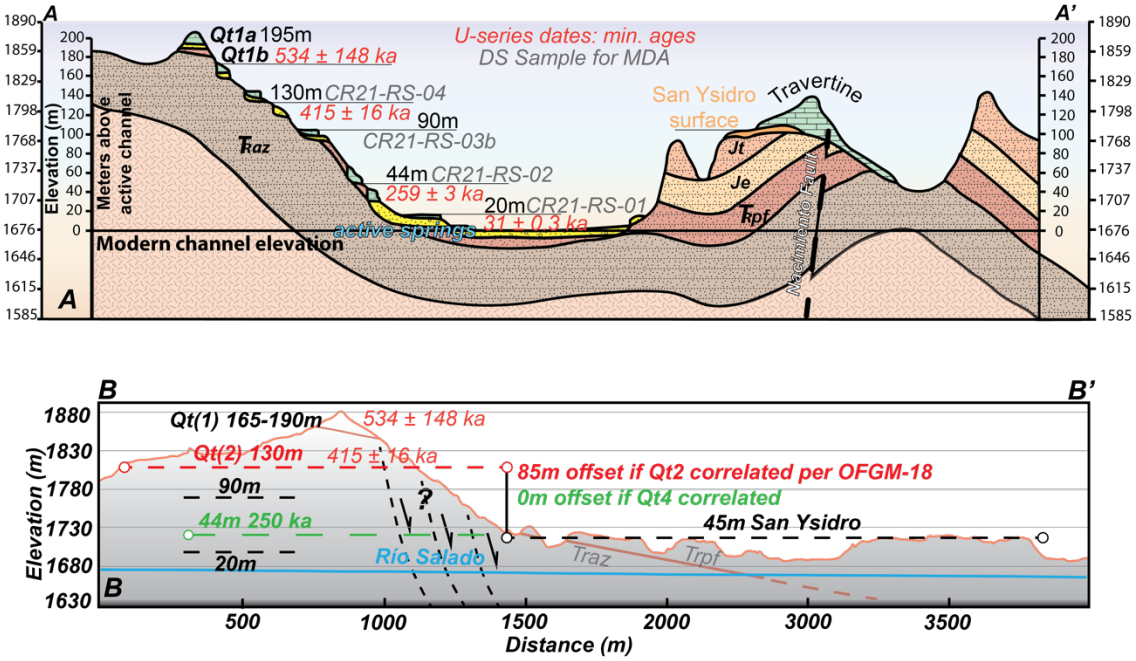

Figure 10: A) Simplified cross section of Río Salado strath terraces with heights determined with 1m lidar. The Triassic Agua Zarca sandstone forms a S-plunging dip-slope on which the terraces are inset. Ages from U-series dated travertine caps and DS MDAs samples are shown with their respective terrace position. The two highest surfaces (designated Qt1a and Qt1b) are outside of U-series range (> 500 ka) and may possibly correlate with the 630 ka Qt1 of La Junta area. The 130m terrace may correlate with the 400 ± 100ka Qt2 of Formento-Trigilio and Pazzaglia (1998) Mapped Qt2 terraces of Formento-Trigilio et al. (1998) are potentially miscorrelated and can easily be supported as Qt4 in an alternative correlation. B) Profile transect of A-A' of Figure 7. Correlated Qt2 terraces are shown between Río Salado (subarea 2) and San Ysidro (subarea 3) in red as mapped by Formento-Trigilio et al. (1998). If the terrace correlation is correct, there is an offset of 85 m across the eastern slope of the Sierra Nacimiento. An alternative correlation is presented in green if the terraces in subarea 3 are supported as Qt4 rather than Qt2. This necessitates no slip across the Towa structure but requires more slip be accommodated by the San Ysidro and Jemez faults between subarea 3 into 5 and 6.

TABLE 1: Table of compiled U-series dates on travertines and $^{40}Ar/^{39}Ar$ DS maximum depositional ages (MDAs) from the Río Salado terraces. K06-SY-67 is a model age. U-series data can be found reported in Cron et al. (this volume).

Terrace height	U-series corrected ages (Cron, 2012)		$^{40}Ar/^{39}Ar$ DS MDA dates (this study)	
20m	K04SY-50	31 ± 0.3 ka	CR21-RS-01	603 ± 15 ka
40m	KOB-SY-63a	250 ± 3 ka	CR21-RS-02	20.5 ± 0.3 Ma
90m			CR21-RS-03b	1.08 ± 0.08 Ma
130m	LC04-SY-5a	415 ± 16 ka	CR21-RS-04	1.164 ± 0.01 Ma
195m	K06-SY-67	534 ± 148 ka		

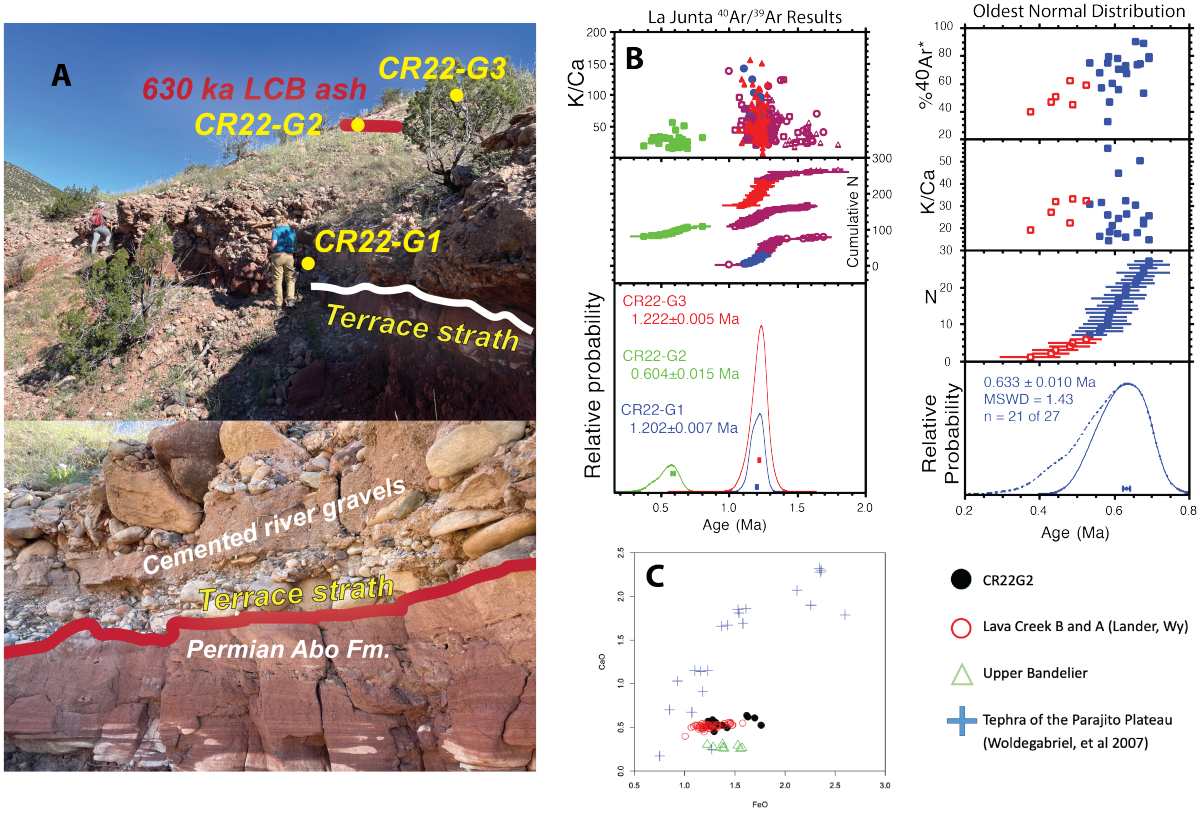

Figure 11: A) Well-exposed bedrock strath cut onto the Abo Formation at base of Qt1 terrace in the La Junta area of subarea 4 (Rogers, 1996; Rogers and Smartt, 1996) and sample locations (yellow) of overlying sands (detrital sanidine and $^{40}Ar/^{39}Ar$ dating) and the Lava Creek B ash (CR22-G2, tephrochronology and $^{40}Ar/^{39}Ar$ dating). B) $^{40}Ar/^{39}Ar$ geochronology of three samples (CR22-G1, 2, 3) are shown on the left plot. The right plot depicts the distribution of 0.4-0.8 Ma ages for the CR22-G2 sample (direct sample of base of ash). In the right plot, (blue squares denote the older normal distribution of CR22-G2 data. The younger normal distribution (red squares) is rejected because the largest population of data better fit the older distribution. The 604 ± 15 ka combined age and 633 ± 10 ka age for CR22-G2 (from the entire 0.4-0.8 Ma distribution and the older normal distribution of CR22-G2, respectively) are within range of expected LCB ash ages. See Supplementary Data for $^{40}Ar/^{39}Ar$ data. C) Glass chemistry results from microprobe analysis of sampled material from CR22-G2 supports a match with LCB tephra compared to tephras derived from the nearby late Pleistocene-Pliocene volcanic centers of the Jemez Mountains.

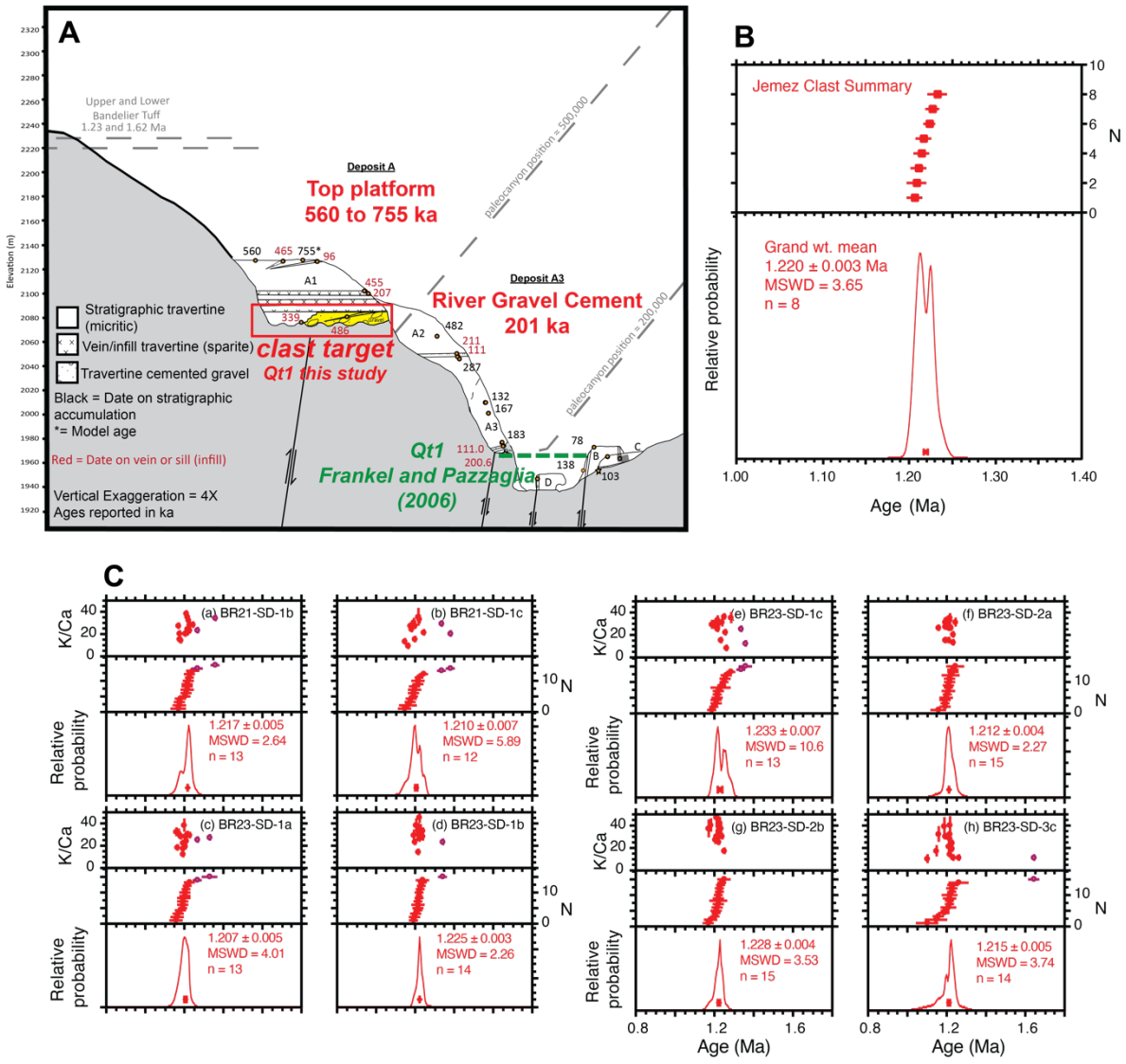

Figure 12: A) Soda Dam travertine ages reported in Tafoya (2012) and Jean et al. (2024).The 150 ARL gravel below deposit A1 is constrained to be older than 560 ka using the younger limit of the micrite at the top of the travertine platform. We sampled rhyolite pebbles in hopes of identifying ~ 550 ka clasts of South Mountain rhyolite and related domes, but all turned out to be Bandelier tuff age (1.22 Ma) with summary ages presented in (B) and individual single grain $^{40}Ar/^{39}Ar$ sanidine analyses for clasts in (C). Other minimum U-series age and the apparent lack of such clasts are consistent with a >550 ka depositional age.

Subarea 5 is the upper Río Jemez near Soda Dam. Terrace correlations between subareas 4 and 5 are complex as the location is reworked by hydrothermal carbonic springs, extensive travertines, and faults of the Jemez fault system. Frankel and Pazzaglia (2006, their Fig. 8) correlated the 90 m ARL Qt1 630 ka terrace of subarea 4 with a 32 m ARL gravel at Soda Dam and concluded that terraces converge upstream on the Río Jemez as a response of base level fall and upstream knickpoint migration. However, Tafoya et al. (2012) and Jean et al. (2024) dated numerous travertine deposits and found that this gravel is cemented by 210 ka travertine making this correlation unlikely, as the difference between depositional age and travertine-cementing age would be ~400 ka in an active travertine setting. Jean et al. (2024) also dated travertine platform A1 that overlies ~150 m ARL gravels near Soda Dam (Fig. 12). The gravel is intruded by a calcite spar sill of 486 ± 25 ka which gives a minimum age. Older but still minimum ages are given by imprecise micrite ages from the top of deposit A1 of 755 ± 212 ka (238U model age) and a U-series age of 568 ± 324 ka. We interpret the gravels to have been cemented near the paleo-river bottom as the travertine developed above them, analogous to the modern stream. If so, this would give a range of incision rates of 200-250 m/Ma or, if the gravels correlate with the Qt1 630 ka terrace from subarea 4, the incision rate would be 238 m/Ma.

Our reasons for interpreting some travertine dates as near-depositional ages for the gravel versus secondary infillings is well illustrated at Soda Dam where we have numerous U-series dates. The interpreted near-primary ages for the 150 m and 31 m gravels is supported by the observation that younger travertine deposits are inset into Deposit A1 and the oldest ages in a given Soda Dam deposit gets progressively younger downward (Fig. 11). The modern setting of travertine-cemented river cobbles at river level provides a good analog for the older deposits. Younger U-series ages of 339-96 ka on sills within deposit A1 are clear examples of secondary

travertine infillings due to episodes of high artesian head as the river incised, with high head potentially due to upstream caldera lakes (Jean et al., 2024). These infilling-type deposits that can form 100s of meters above river base level as also seen in the Tierra Amarilla anticline (Cron et al., 2024) where artesian waters currently move up semi-confined fault conduits.

The proposed 268 m/Ma incision rate at Soda Dam over the past 560 Ma (Fig. 11) is more precise than warranted by the imprecise geochronology but if we use a range of ages of 563-755 ka, this results in a range of incision rates (268-199 m/Ma) that is ~50-100 m/Ma higher than the 143 m/Ma rate in subarea 4 at La Junta. This is interpreted as due to W-up displacement on the Jemez fault zone. This scale of differential incision is compatible with the ~380 m height above river level (ARL) of the base of the 1.62 Ma Otowi Member of the Bandelier Tuff in this area. Using the height and age of the Otowi Member gives a long-term average bedrock incision rate of 235 m/Ma since 1.62 Ma, or 309 m/Ma from the base of the 1.2 Ma Bandelier Tuff (in this area, was little bedrock incision (canyon deepening) between the 1.62 and 1.23 Ma Bandelier Tuff eruptions). These rates are >100 m/Ma higher than those in Subarea 4 where the long-term bedrock incision rate has been steady at 140-150 m/Ma since 1.23 Ma based on gravels coeval with and at the base of the upper Bandelier Tuff (Qg2 and Qg3 of Rogers and Smart, 1996) and based on the 90 m ARL Qt1 terrace that contains the 0.63 Ma Lava Creek B ash. Correlating the 150m ARL Soda Dam gravels with the 90 m/Ma LCB gravels downstream, the associated terrace level (Qt1) appears to diverge upstream rather than converge (Frankel and Pazzaglia, 2005) which is compatible with headwater uplift.

Discussion Of Differential Incision Across Faults

We explore the Formento-Trigilio and Pazzaglia (1996) model that differences in incision relative to correlated terrace straths is observed across faults and can be used to estimate fault

slip. They did not consider our subareas 2 and 5 and concluded that fault slip on the Nacimiento and Cross Valley faults was an order of magnitude (13 m/Ma) less then river incision (171 m/Ma). They inferred fault offsets between subareas, but their fault slip rate did not include what we think may be some major Quaternary faults and their river incision rate assumed steady incision across the different areas and did not have the advantage of an as extensive geochronology dataset.

Our discussion of inferred fault vertical offsets is summarized in Figures 8 and 9. We use the highest terrace sets, Qt1 and Qt2. Our preferred correlation for Qt1 from the dated terraces is that the 90 m ARL, 630 ka, Qt1 LCB terrace in subarea 4 is approximately the same age as the 164 m ARL, 534 ± 164 ka, Qt1b terrace in subarea 2 and the 150 ARL, 500-700 ka, Qt1 gravels at Soda Dam. Even though the analytical error on the U-series model ages in subareas 2 and 5 is large (± 150 ka), the ages are compatible with other nearby dates that are within U-series range. The Qt2 terrace correlation relies on earlier mapping and directly tying the ~400 ka age from the travertine in subarea 2 with inferred 400-500 ka age terraces in subarea 4. Both the Qt1 and Qt2 correlations use our assumption that the aforementioned U-series ages of travertine are near-depositional ages.

Using round numbers for the long-term rates to recognize the dating uncertainties, the large height differences in age-similar terraces equates to differential incision along the river system of ~150 m/Ma between subarea 4 (150 m/Ma) and subarea 2 (~ 300 m/Ma) and about 100 m/Ma between subarea 4 (150 m/Ma) and subarea 5 (~250 m/Ma). Given the short distance between areas, the relatively smooth concave-up profiles, low k_{sn} values of the Arroyo Peñasco, Río Salado and lower Río Jemez river system (Rogers, 1996; Formento-Trigilio and Pazzaglia, 1998; Frankel and Pazzaglia, 2005), and known presence of Quaternary faulting, the differential

incision is interpreted here to reflect slip on Quaternary faults with subarea 4 down dropped relative to subareas 2 and 5. For the approximately 600 ka terraces (Qt1), we infer up to 75 m of E-down slip between subareas 2 and 4 and 60 m between subareas 4 and 5. Bedrock incision rates were steady back at least to 1.2 Ma in for subareas 4 and 5 implying that there has been long-lived faulting due to tectonic uplift of the Jemez Mountains and Sierra Nacimiento and/or subsidence of the Río Grande rift.

More detailed parsing of the Quaternary fault slip on the different structures between the subareas depends on uncertain terrace correlations that requires more refined geochronology. Nevertheless, for the major displacements, we infer that ~ 100 m/Ma of S-down slip has taken place between subareas 4 and 5 across the Jemez fault zone over the past 1.2 Ma. If the published correlations of Qt1 and Qt2 from Formento-Trigilio (1997), Formento-Trigilio et al. (1998), and Formento-Trigilio and Pazzaglia (1998) are correct (alternative 1), most of the ~ 85 m offset between subareas 2 and 4 takes place on the enigmatic Towa structure. However, if the subarea 3 terraces correlate with the 250 ka Qt4 instead of the 400 ka Qt2 of subarea 2 (alternative 2), then slip on the Towa structure was zero or minimal and the 60 m of differential incision was accommodated by slip was on the San Ysidro and Jemez faults.

Our data between subareas also provide preliminary estimates of differential incision at the 10s of meters scale (Fig. 9) that hints the presence of a network of small N-S and NE-striking fault segments with distributed Quaternary displacements. Subareas 1 and 2 are not sufficiently well correlated to refine the estimate of Formento-Trigilio and Pazzaglia (1998) of the Quaternary slip on the Nacimiento fault for which they reported a 17-m high fault scarp, and a knickpoint on the Arroyo Peñasco that coincides with a segment of the Nacimiento fault with young (<250 ka) faulting, and an inferred slip rate of ~10 m/Ma. The Cross Valley fault of

Formento-Trigilio and Pazzaglia (1998) cuts between the terraces at San Ysidro (subarea 3) and Walatowa (subarea 4) but the difference in terrace heights can be also explained by E-down displacement on the San Ysidro fault. Comparing differences in terrace heights between subarea 6 (Zia) and subarea 2 (San Ysidro) across the San Ysidro fault exhibit 10-15m-scale differences in heights, depending on how they are correlated, consistent with the 11 m of offset across the San Ysidro-Jemez fault interpreted by Formento-Trigilio and Pazzaglia (1998).

Incision Rates Through Time

There is enough age control on higher surfaces and lower terraces in addition to Qt1 and Qt2 to begin to investigate whether rates were semi-steady through time within each terrace sub-area. To do this, we also use the height of Bandelier Tuff units of known age as shown in Figure 12 for Cañon de San Diego. Cañon de San Diego existed as a canyon before the eruptions of the 1.62 and 1.23 Ma Bandelier tuffs (Turbeville and Self, 1988; Hulen et al., 1991; Rogers et al., 1996; Kelley et al., 2007) that filled and preserved pre-eruption topography shown in Figure 13. There are also gravels below the Bandelier Tuffs that preserve a record of pre-1.62 Ma river systems (Rogers, 1996; Smith and Lavine, 1996; Kelley et al., 2007). There was no significant denudation in the San Diego Canyon area between the two eruptions such that the lower and upper Bandelier Tuff are generally stacked on top of one another in a single cliff (Fig. 13). From the viewpoint of bedrock incision, the tuffs might be considered fill material similar to fill terraces. If so, the height of the base of the 1.62 Ma Otowi Member cliff above the modern Río Jemez provides a long-term bedrock incision (canyon deepening) rate for Cañon de San Diego (solid line in Fig. 13A). Considering that the river had to also re-incise through ignimbrite fill, the dashed line in Figure 13 reflects incision rates as measured from the top of the 1.23 Bandelier Tuff (Fig. 13B). The dashed line rates are significantly higher as expected because of rivers

adjusting to grade following a major perturbation to the landscape (i.e., sudden emplacement of a >100 m thick ignimbrite).

Near the confluence of the Río Guadalupe and Río Jemez (La Junta), Rogers (1996) identified 3 well-dated buried gravels in the canyon walls. The oldest of these, Qg1, is exposed underneath 1.62 Ma Otowi member (LBT) on the sides of Virgin Mesa, Mesa de las Casas, and Guadalupita Mesa approximately 192 m ARL, yielding an estimated incision rate of 119 m/Ma from 1.62 Ma to present. Qg2 is an axial stream gravel that lies approximately 187 m ARL at the southern end of Mesa de Guadalupe and is buried by the basal pumice fall (Tsankawi Pumice) of the 1.23 Ma Tshirege Member (UBT) yielding an incision rate of 152 m/Ma since 1.23 Ma. Qg3, an axial gravel buried directly beneath the Tsankawi pumice, approximately 176 m ARL, was interpreted to be the actual flowing stream at the time of the 1.23 Ma Tshirege eruption (whereby the Qg2 gravel occupied a paleo-terrace). This channel deposit contains Tsankawi pumice that was being deposited as crossbedded fluvial pumice bars in the active channel during the eruption until the stream succumbed to the ash flows of the UBT. Incision near La Junta from the Qg3 exposure provides an incision rate of 143 m/Ma since 1.23 Ma, similar to the 152 m/Ma rate calculated from Qg2 and the same as the post-630 ka rate of 143 m/Ma. We prefer this ~143 m/Ma rate to the 171 m/Ma reported by Formento-Trigilio and Pazzaglia (1998, their Fig. 5) that was based on a regression line that assumed steady incision between 1.2 and 0.3 Ma, but we agree that this subarea records steady rates of bedrock incision since 1.62 Ma. Soda Dam (subarea 5) also show steady long-term average bedrock incision, but at different rates than the 143 m/Ma seen in subarea 4. At Soda Dam rates were 247 m/Ma since 1.62 and ~250 m/Ma assuming a ~ 600 ka age for the 150 ARL m gravels. At Río Salado, rates were 307-313 for both Qt1 and Qt2 (Fig. 9 Qt1).The apparent semi-steady long-term average bedrock incision rates

within these two subareas over the 1.6-0.4 Ma timeframes is consistent with broad epeirogenic uplift of the Jemez Mountains regions rather than headward-propagating knickpoints responding to base level fall (Frankel and Pazzaglia, 2006). Rogers (1996) concluded that incision has been unsteady through time, with low rates (40 m/Ma) between 1.62 and 1.23 Ma, but this was considering the incision that followed the emplacement of the Otowi and Tshirege Members compared to young terraces near the modern channel. His reported average for post-LCB incision rate of ~150 m/Ma used the terrace tread height of 111 m (rather than the 90 m strath height) and an LCB age of 620 ka (rather than 630 ka) but is very similar to our 143 m/Ma rate. Formento-Trigilio and Pazzaglia's (1998) interpreted that average bedrock incision rates were steady at 171 m/Ma based on a regression line through points with significant error bars for both age and height which is broadly similar to our 143 m/Ma estimate. They interpreted an increase to short-term rates of 180 m/Ma after their 150 ka Qt4. Because differential incision between subareas is seen both at 1.62 Ma, 1.23 Ma, and 630 ka timeframes, that average out short term variations, we infer that the difference of 164 and 92 m/Ma for Qt1 between subareas 2 and 5, respectively, and subarea 4, seems best interpreted as due to fault-influenced incision.

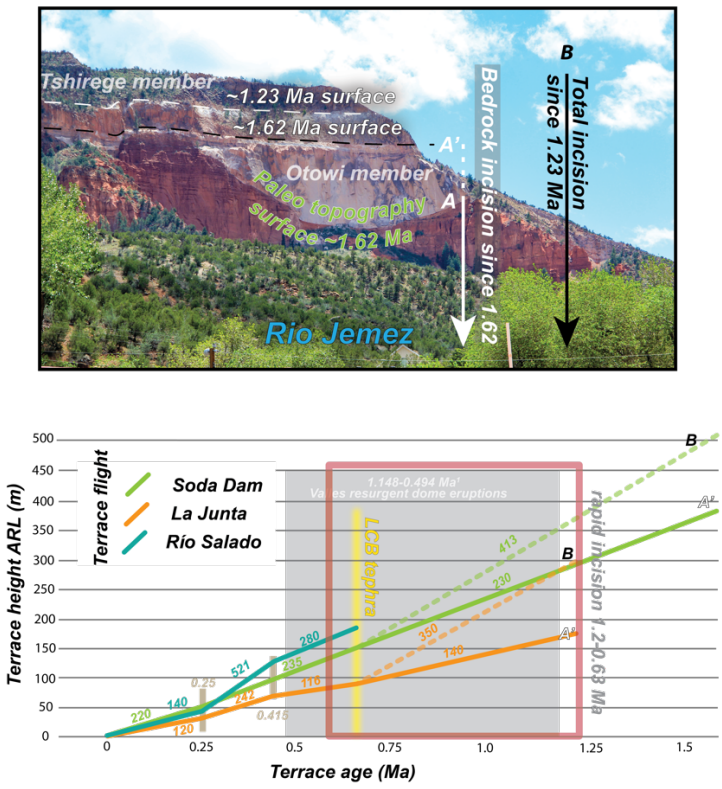

Figure 13: Top plot: Paleotopography of Cañon de San Diego is preserved by the 1.62 Ma Otowi member whereby the bottom of the Bandelier cliff often is near the top of the 1.62 Ma surface representing a close approximation to bedrock incision since 1.62 Ma. The top of the Tshirege member provides an estimate of the total incision done by the Río Jemez since 1.23 Ma. Bottom plot: Incision rates through time are shown for three keys terrace flights: subarea 2- Río Salado on the nose of the Sierra Nacimiento; subarea 4- La Junta; and subarea 5- Soda Dam. For Bandelier Tuff- constrained incision rates, heights are reported in two ways: 1, from the base of the 1.62 Ma tuff (solid lines marked B) that consider the tuffs like aggregational terraces, hence measure bedrock incision (canyon deepening) since 1.62 Ma, 2) from the top of the 1.23 Ma upper Bandelier Tuff (dashed line) that also includes incision of the tuffs. Paleotopography of Cañon de San Diego is preserved by Otowi Member fill. Rapid incision between 1.23 and 0.630 Ma on the graph reflects topographic resetting processes following widespread deposition of thick ignimbrite and caldera sequences.

Figure 13A shows two conceptualizations for calculating long-term rates using the Bandelier Tuffs. The deepest point of paleo Cañon de San Diego is not well exposed but preserved paleochannel remnants are tens of meters deep (A of Fig 13A) such that this amount could be, but is usually not, added to the calculation that uses the well exposed base of the 1.62 Ma Otowi and 1.23 Tshirege Members as regional surfaces (A' in Fig. 13A). The solid lines in

Figure 12B plot bedrock incision (the A' method) and consider the tuffs to be like "fill terraces" that are not included when strath heights are used. The dashed lines plot total incision (the B method) that the river had to accomplish to cut through the tuffs to resume bedrock incision (deepening) of San Diego Canyon. Both curves come together at ~ 600 ka, the beginning of the terrace record. The result in Figure 12B shows semi-steady rates through time for the past ~ 600 ka in each subarea (even given possible accelerated short term rates after 150-200 ka) but with rates that differ significantly between subareas at both 1.2 Ma and ~600 ka timescales.

Caveats and Limitations of Terrace Correlations and Ages

Limitations of most terrace studies include incomplete terrace age data and incomplete preservation that make terrace correlations difficult. Here, we have relied on and refined the Formento-Trigilio and Pazzaglia (1998) Qt1 and Qt 2 correlations and extended this correlation to include the highest terraces in two new subareas, at Río Salado and Soda Dam. In both areas, the >500 ka "beyond U-series" results for the highest terraces coupled with imprecise $\delta^{234}U$ model ages and constraints from lower terraces within a given subarea are compatible with the notion, but not definitive, that our highest terraces in each area may be similar in age to the 630 ka Qt1 terrace at La Junta. Our age of 415 ka for Qt2 terraces are compatible with prior workers who estimated a ~400 ka age based on other techniques (Rogers and Smartt, 1996; Rogers, 1996; Formento-Trigilio and Pazzaglia, 1998). This correlation leads to our proposed Quaternary fault offsets but better ages across multiple flights of terraces are needed to continue to test this idea using U-Pb, luminescence (IRSL) dating (Nelson et al., 2015; Mahan et al., 2022), and detrital sanidine.

In the alternative 1 published correlation, the 85 m of proposed Qt2 offset (85 m) implied by our proposed correlations between the Río Salado (subarea 2) and San Ysidro (subarea 3)

terraces is high especially because the fault has been previously unmapped. This motivates the alternative 2 interpretation. For example, the 415 ka Rio Salado Qt2 terrace in subarea 2 might be correlated with the 45m terrace of subarea 3, but this would still entail a significant 45m offset between these terraces (rather than 85m). If one used only heights ARL for correlation, the Qt2 terrace of Formento-Trigilio and Pazzaglia in subareas 1 and 3 might be correlated to the 40m terrace in our subarea 2 terraces that has a U-series age of 259 ka and if so, higher terraces are not preserved and the correlation around the corner to the 630 ka terrace on the Río Jemez in subarea 4 is incorrect. The age constraints from terrace fills are minimum dates for the age of the underlying strath, even for the Lava Creek B-aged terrace. This is an uncertainty in all terrace studies. It is usually assumed that terrace fills closely follow straths during ~100 ka aggradation/incision climate oscillations and river response (Pazzaglia, 2013) but younger terraces can overtop older terraces. Similarly, we use the still-active travertine systems themselves as analogs that gravels are cemented by contemporaneous travertine such that the U-series dates are near-direct dates. Younger terraces (like Qt2-3) can potentially over-top older terraces as noted by Formento-Trigilio and Pazzaglia (1998) further complicating correlation and mapping efforts. Nevertheless, there is enough uncertainty in the dating and large gaps in preservation of the terraces in many of the subareas that alternative correlations may reduce or erase our proposed differential incision across faults once more date are obtained for more terraces in each flight. Additionally, the role of dipping bedrock and bedrock erodibility (Darling et al., 2020; Mitchell and Yanites, 2021) needs to be further investigated as a driver for apparent high incision rates at Río Salado and Soda Dam relative to the La Junta confluence area.

CONCLUSIONS

The conclusion of this paper is that the bedrock incision rate data for the Jemez River system at the 0.4 to 1.6 Ma timescale provide a convincing case for overall steady incision history within each reach but ~100 m/Ma-scale differential bedrock incision between reaches that are separated by faults. This is based on the two highest mapped terraces in each of 6 areas of intact terrace flights that are preserved "around the corner" from the west side of the Nacimiento fault on the Arroyo Peñasco, along the Río Salado, and up the Río Jemez from San Ysidro to Soda Dam on the Jemez fault zone. New U-series geochronology shows that the uppermost terrace (Qt1) in Río Salado terrace flight (subarea 2) and near Soda Dam (subarea 5) are both outside of U-series range (>500 ka) but give $\delta^{234}U$ model ages of 465-755 ka and hence are permissively correlated with the Lava Creek B ash (630 ka) Qt1 terrace near the confluence of the Río Jemez and Guadalupe (subarea 4). Our preferred correlation of an underlying terrace is based on relating a U-series age of 415 ka at Rio Salado with a ~400 ka age estimates from soil profiles of Qt2 (Formento-Trigilio, 1997) from the confluence area.

If these correlations are correct, the Qt1 and Qt2 straths can be used in tandem to infer different incision rates in the different subareas. This equates to differential incision rates of ~ 100-150 m/Ma along the river system: ~150 m/Ma between subareas 2 and 4 and ~ 100 m/Ma between subareas 4 and 5. Given the short distances between the areas, the relatively smooth concave-up profiles of both the Río Salado and Río Jemez, and known presence of Quaternary faulting, this differential incision is interpreted to reflect slip on Quaternary faults. If so, subarea 4 has been down-dropped relative to subareas 2 and 5. For the ~600 ka timeframe, ~74 m of E-down slip between subareas 2 and 4 and ~60 m between subareas 4 and 5. We acknowledge other possible correlations, which would change these slip rates.

Proposed tectonic influences on river evolution include fault-influenced incision where upthrown blocks have higher incision rates than downthrown blocks and where the difference is interpreted to be due mainly to fault displacement. If so, the inferred rates of Quaternary fault displacement are ~ 160 m/Ma between subareas 2 and 4 over the past ~600 ka and hence similar in magnitude to river incision rates, suggesting that the block uplift has a significant influence on river incision. The faulting itself may be related to rift extension and a broader scale of epeirogenic surface uplift of the combined Sierra Nacimiento-Jemez Mountain areas. The latter is suggested by topographic analysis and by our interpreted upstream -diverging terraces on the Río Jemez that suggest that headwater uplift may be interacting with base-level fall in the Río Grande system at the million-year timescale. Improved terrace geochronology is needed to improve assessment of the magnitude of Quaternary fault displacements in what appears to be a distributed fault network that is elevating the Nacimiento and Jemez Mountain blocks relative to the adjacent Colorado Plateau and Río Grande rift provinces.

References

Aldrich, M.J., 1986, Tectonics of the Jemez lineament in the Jemez Mountains and Rio Grande Rift (USA).: Journal of Geophysical Research, v. 91, p. 1753–1762, doi:10.1029/JB091iB02p01753.

Anderson, J.C., Karlstrom, K.E., and Heizler, M.T., 2021, Neogene drainage reversal and Colorado Plateau uplift in the Salt River area, Arizona, USA: Geomorphology, v. 395, p. 107964, doi:10.1016/j.geomorph.2021.107964.

Armstrong, I.P., Yanites, B.J., Mitchell, N., DeLisle, C., and Douglas, B.J., 2021, Quantifying Normal Fault Evolution from River Profile Analysis in the Northern Basin and Range Province, Southwest Montana, USA: Lithosphere, v. 2021, p. 7866219, doi:10.2113/2021/7866219.

Aslan A, Karlstrom K, Kirby E, Heizler M, Granger D.E., Feathers J.K., Hanson P.R., and Mahan S.A., 2019, Resolving time-space histories of Late Cenozoic bedrock incision along the Upper Colorado River, USA: Geomorphology, v. 347.

Bridgland, D., & Westaway, R. (2008). Climatically controlled river terrace staircases: a worldwide Quaternary phenomenon. Geomorphology, 98(3-4), 285-315.

Bull, William B. "Geomorphic responses to climatic change." (1991).

Cather, S.M., Chapin, C.E., and Kelley, S.A., 2012, Diachronous episodes of Cenozoic erosion in southwestern North America and their relationship to surface uplift, paleoclimate, paleodrainage, and paleoaltimetry: Geosphere, v. 8, p. 1177–1206, doi:10.1130/GES00801.1.

Channer, M.A., Ricketts, J.W., Zimmerer, M., Heizler, M., and Karlstrom, K.E., 2015, Surface uplift above the Jemez mantle anomaly in the past 4 Ma based on 40Ar/39Ar dated

paleoprofiles of the Rio San Jose, New Mexico, USA: Geosphere, v. 11, p. 1384–1400, doi:10.1130/GES01145.1.

Chapin, C.E., Wilks, M., McIntosh, W.C., 2004, Space-time patterns of Late-Cretaceous to present magmatism in New Mexico—Comparison with Andean volcanism and potential for future volcanism, in Cather, S.M., McIntosh, W.A., Kelley, S.A., eds., Tectonics, Geochronology, and Volcanism in the Southern Rocky Mountains and the Rio Grande Rift: New Mexico Bureau of Geology and Mineral Resources Bulletin 160 , p. 13–40.

Cikoski, C.T., and Koning, D.J., 2017, Deep-seated landslide susceptibility map of New Mexico: New Mexico Bureau of Geology and Mineral Resources Open-file Report OFR-594

Cox, C., Kelley, S. A., Karlstrom, K. E., Crossey, L., Dillon, M. & Newell, D. 2005. Quaternary Incision History of the Upper Reaches of the Jemez River. New Mexico Geology, 27, 43.

Cron, B., 2012, Geochemical Characteristics and Microbial diversity of CO 2-rich mound springs of the Tierra Amarilla anticline, New Mexico.

Cron, B., Crossey, L.C., Karlstrom, K.E., Polyak, V., Asmerom, Y., and McGibbon, C, 2024, Geochemistry and microbial diversity of CO2-rich springs and U-series dating of travertine from the Tierra Amarilla anticline, New Mexico: *in* Karlstrom, K.E., Koning, D.J., Lucas, S.G., Iverson, N.A., Crumpler, L.S., Aubele, J.C., Blake, J.M., Goff, F., and Kelley, S.A., eds., Geology of the Nacimiento Mountains and Río Puerco Valley: New Mexico Geological Society Guidebook 74 (this volume), p. XXX–XXX. =

Crow, R., Karlstrom, K., Darling, A., Crossey, L., Polyak, V., Granger, D., Asmerom, Y., and Schmandt, B., 2014, Steady incision of Grand Canyon at the million year timeframe: A case for mantle-driven differential uplift: Earth and Planetary Science Letters, v. 397, p. 159–173, doi:10.1016/j.epsl.2014.04.020.

Darling, A., Whipple, K., Bierman, P., Clarke, B., and Heimsath, A. (2020) Resistant rock layers amplify cosmogenically-determined erosion rates. *Earth Surf. Process. Landforms*, 45: 312–330. https://doi.org/10.1002/esp.4730.

Dethier, D.P., 2001, Pleistocene incision rates in the western United States calibrated using Lava Creek B tephra: Geology, v. 29, p. 783, https://doi.org/10.1130/0091-7613(2001)029<0783:PIRITW>2.0.CO;2.

Formento-Trigilio, M. L., 1997, Soil-landscape relation-Chapin, C. E., and Cather, S. M., 1983, Eocene tectonicsand sedimentation in the Colorado Plateau–Rockyships in the Jemez River drainage basin, northern NewMexico: Unpub. M.S. thesis, Albuquerque, University

Formento-Trigilio, M., Toya, C., and Pazzaglia, F., 1998, Preliminary Geologic Map of the San Ysidro Quadrangle OF-GM 18, Sandoval County, New Mexico. https://doi.org/10.58799/OF-GM-18

Formento-Trigilio, M.L., and Pazzaglia, F.J., 1998, Tectonic Geomorphology of the Sierra Nacimiento: Traditional and New Techniques in Assessing Long-Term Landscape Evolution in the Southern Rocky Mountains 1: The Journal of Geology, v. 106, p. 433–453. https://doi.org/10.1086/516034

Frankel, K.L., and Pazzaglia, F.J., 2006, Mountain fronts, base-level fall, and landscape evolution: Insights from the southern Rocky Mountains, *in* Willett, S.D., Hovius, N., Brandon, M.T., and Fisher, D.M. eds., Tectonics, Climate, and Landscape Evolution, Geological Society of America, v. 398, p. 0, doi:10.1130/2006.2398(26).

Gallen, S.F., and Wegmann, K.W., 2017, River profile response to normal fault growth and linkage: an example from the Hellenic forearc of south-central Crete, Greece: Earth Surface Dynamics, v. 5, p. 161–186, doi:10.5194/esurf-5-161-2017.

Heizler, M.T., Karlstrom, K.E., Albonico, M., Hereford, R., Beard, L.S., Cather, S.M., Crossey, L.J., and Sundell, K.E., 2021, Detrital sanidine 40Ar/39Ar dating confirms <2 Ma age of Crooked Ridge paleoriver and subsequent deep denudation of the southwestern Colorado Plateau: Geosphere, v. 17, p. 438–454, doi:10.1130/GES02319.1.

Hobson, R. D. 1972. Surface roughness in topography: quantitative approach. In *Spatial analysis in geomorphology* (pp. 221-246). Routledge.

Howard, A.D., Dietrich, W.E., and Seidl, M.A., 1994, Modeling fluvial erosion on regional to continental scales: Journal of Geophysical Research: Solid Earth, v. 99, p. 13971–13986, doi:10.1029/94JB00744.

Hulen, J. B., D. L. Nielson, and T. M. Little (1991), Evolution of the Western Valles Caldera Complex, New Mexico: Evidence from intracaldera sandstones, breccias, and surge deposits, *J. Geophys. Res.*, 96(B5), 8127–8142, doi:10.1029/91JB00374.

Jaiswara, N.K., Kotluri, S.K., Pandey, P., and Pandey, A.K., 2020, MATLAB functions for extracting hypsometry, stream-length gradient index, steepness index, chi gradient of channel and swath profiles from digital elevation model (DEM) and other spatial data for landscape characterisation: Applied Computing and Geosciences, v. 7, p. 100033, doi:10.1016/j.acags.2020.100033.

Jean, A., Crossey, L.J., Karlstrom, K.E., Polyak, V., and Asmerom, Y., 2024, Uranium-series geochronology of travertine from Soda Dam, New Mexico: A Quaternary record of episodic spring discharge and river incision in the Jemez Mountains, *in* Karlstrom, K.E., Koning, D.J., Lucas, S.G., Iverson, N.A., Crumpler, L.S., Aubele, J.C., Blake, J.M., Goff, F., and Kelley, S.A., eds., Geology of the Nacimiento Mountains and Río Puerco Valley: New Mexico Geological Society Guidebook 74 (this volume), p. XXX–XXX.

Jicha, B.R., Singer, B.S., and Sobol, P., 2016, Re-evaluation of the ages of 40Ar/39Ar sanidine standards and supereruptions in the western U.S. using a Noblesse multi-collector mass spectrometer: Chemical Geology, v. 431, p. 54–66, doi:10.1016/j.chemgeo.2016.03.024.

Karlstrom, K.E. et al., 2012, Mantle-driven dynamic uplift of the Rocky Mountains and Colorado Plateau and its surface response: Toward a unified hypothesis: Lithosphere, v. 4, p. 3–22, doi:10.1130/L150.1.

Karlstrom, K.E., Crossey, L.J., Embid, E., Crow, R., Heizler, M., Hereford, R., Beard, L.S., Ricketts, J.W., Cather, S., and Kelley, S., 2016, Cenozoic incision history of the Little Colorado River: Its role in carving Grand Canyon and onset of rapid incision in the past ca. 2 Ma in the Colorado River System: Geosphere, v. 13, p. 49–81, doi:10.1130/GES01304.1.

Karlstrom, K.E., Crow, R., Crossey, L.J., Coblentz, D., and Wijk, J.W.V., 2008, Model for tectonically driven incision of the younger than 6 Ma Grand Canyon: Geology, v. 36, p. 835–838, doi:10.1130/G25032A.1.

Karlstrom, K.E., Crow, R.S., Peters, L., McIntosh, W., Raucci, J., Crossey, L.J., Umhoefer, P., and Dunbar, N., 2007, 40Ar/39Ar and field studies of Quaternary basalts in Grand Canyon and model for carving Grand Canyon: Quantifying the interaction of river incision and normal faulting across the western edge of the Colorado Plateau: GSA Bulletin, v. 119, p. 1283–1312, doi:10.1130/0016-7606(2007)119[1283:AAFSOQ]2.0.CO;2.

Karlstrom, K.E., Koning, D., Lucas, S.G., Crumpler, L.S., Goff, F., Kelley, S., Iverson, N., Reed, C., and Crossey, L.J., 2024, Synopsis of the San Ysidro geologic nexus, *in* Karlstrom, K.E., Koning, D.J., Lucas, S.G., Iverson, N.A., Crumpler, L.S., Aubele, J.C., Blake, J.M.,

Goff, F., and Kelley, S.A., eds., Geology of the Nacimiento Mountains and Río Puerco Valley: New Mexico Geological Society Guidebook 74 (this volume), p. XXX–XXX.

Kelley, S. A., Goff, F., Miller, P. L., Sawyer, D. A., Koning, D. J., Thompson, R. A., ... & Jochems, A. P. (2023). Geologic Map of the Los Alamos 30 x 60-Minute Quadrangle, 1: 24,000 Scale Compilation of the Los Alamos, Rio Arriba, Santa Fe, and Sandoval Counties, New Mexico.

Kelley, S.A., Osburn, R.G., and Kempter, K.A., 2007, Geology of Canon de San Diego, southwestern Jemez Mountains, north-central New Mexico, *in* Geology of the Jemez Region II, New Mexico Geological Society, p. 169–181, doi:10.56577/FFC-58.169.

Kelley, V. C. (1977). Geology of Albuquerque Basin, New Mexico. https://doi.org/10.58799/M-33

Kirby, E., and Whipple, K.X., 2012, Expression of active tectonics in erosional landscapes: Journal of Structural Geology, v. 44, p. 54–75, doi:10.1016/j.jsg.2012.07.009.

Love, D.W., Connell, S.D., and Lucas, S., 2005, Late Neogene drainage developments on the southeastern Colorado Plateau, New Mexico: N Mex Mus Nat Hist Sci Bull, v. 28, p. 151–169.

Magnani, M.B., Miller, K.C., Levander, A., and Karlstrom, K., 2004, The Yavapai-Mazatzal boundary: A long-lived tectonic element in the lithosphere of southwestern North America: Geological Society of America Bulletin, v. 116, p. 1137, doi:10.1130/B25414.1.

McCalpin, J.P., Harrison, J.B.J., Berger, G.W., and Tobin, H.C., 2011, Paleoseismcity of a low slip-rate normal fault in the Rio Grande rift, USA: The Calabacillas fault, Albuquerque, New Mexico, in Audemard, F.A.A., Michetti, A.M., and McCalpin, J.P., eds., Geological

Criteria for Evaluating Seismicity Revisited: Forty Years of Paleoseismic Investigations and the Natural Record of Past Earthquakes, https://doi.org/10.1130/SPE479

Merrihue, C., and Turner, G., 1966, Potassium-argon dating by activation with fast neutrons: Journal of Geophysical Research (1896-1977), v. 71, p. 2852–2857, doi:10.1029/JZ071i011p02852.

Mitchell, N.A., and Yanites, B.J., 2021, Bedrock river erosion through dipping layered rocks: quantifying erodibility through kinematic wave speed: Earth Surface Dynamics, v. 9, p. 723–753, doi:10.5194/esurf-9-723-2021.

Nasholds, M.W.M., and Zimmerer, M.J., 2022, High-precision 40Ar/39Ar geochronology and volumetric investigation of volcanism and resurgence following eruption of the Tshirege Member, Bandelier Tuff, at the Valles caldera: Journal of Volcanology and Geothermal Research, v. 431, p. 107624, doi:10.1016/j.jvolgeores.2022.107624.

Nelson, M. S., Gray, H. J., Johnson, J. A., Rittenour, T. M., Feathers, J. K., & Mahan, S. A. (2015). User guide for luminescence sampling in archaeological and geological contexts. Advances in Archaeological Practice, 3(2), 166-177. https://doi.org/10.7183/2326-3768.3.2.166

Nereson, A., Stroud, J., Karlstrom, K., Heizler, M., and McIntosh, W., 2013, Dynamic topography of the western Great Plains: Geomorphic and 40Ar/39Ar evidence for mantle-driven uplift associated with the Jemez lineament of NE New Mexico and SE Colorado: Geosphere, v. 9, p. 521–545, doi:10.1130/GES00837.1.

Ohmori, H., 1993, Changes in the hypsometric curve through mountain building resulting from concurrent tectonics and denudation: Geomorphology, v. 8, p. 263–277, doi:10.1016/0169-555X(93)90023-U.

Pazzaglia, F. J. 9.23 Fluvial Terraces. *Treatise of Geomorphology, edited by: Wohl, E., Elsevier, Amsterdam, the Netherlands*. 2013

Pazzaglia, F. J., Pederson, J. L., Garcia, A., Koning, D., and Toya, C., 1997, Geologic map and report of the Jemez Pueblo quadrangle, NM: New Mexico Bureau of Mines and Mineral Resources, scale 1:24,000.

Pederson, J., Karlstrom, K., Sharp, W., and McIntosh, W., 2002, Differential incision of the Grand Canyon related to Quaternary faulting—Constraints from U-series and Ar/Ar dating: Geology, v. 30, p. 739–742, doi:10.1130/0091-7613(2002)030<0739:DIOTGC>2.0.CO;2.

Perkins, M.E., Nash, W.P., Brown, F.H., and Fleck, R.J., 1995, Fallout tuffs of Trapper Creek, Idaho—A record of Miocene explosive volcanism in the Snake River Plain volcanic province: Geological Society of America Bulletin, v. 107, p. 1484–1506. doi: 10.1130/0016-7606(1995)107<1484:FTOTCI>2.3.CO;2

Perron, J.T., and Royden, L., 2013, An integral approach to bedrock river profile analysis: INTEGRAL APPROACH TO RIVER PROFILE ANALYSIS: Earth Surface Processes and Landforms, v. 38, p. 570–576, doi:10.1002/esp.3302.

Pike, R.J., and Wilson, S.E., 1971, Elevation-relief ratio, hypsometric integral, and geomorphic area-altitude analysis: Geological Society of America Bulletin, v. 82, p. 1079–1084.

Purinton, B., and Bookhagen, B., 2017, Validation of digital elevation models (DEMs) and comparison of geomorphic metrics on the southern Central Andean Plateau: Earth Surface Dynamics, v. 5, p. 211–237, doi:10.5194/esurf-5-211-2017.

Reneau, S. L., Drakos, P. G., & Katzman, D. (2007). Post-resurgence lakes in the Valles caldera, New Mexico. Geology of the Jemez region II: New Mexico Geological Society, Guidebook, 58, 398-408.

Repasch, M., Karlstrom, K., Heizler, M., and Pecha, M., 2017, Birth and evolution of the Rio Grande fluvial system in the past 8 Ma: Progressive downward integration and the influence of tectonics, volcanism, and climate: Earth-Science Reviews, v. 168, p. 113–164, doi:10.1016/j.earscirev.2017.03.003.

Riley, S.J., DeGloria, S.D., and Elliot, R., 1999, Index that quantifies topographic heterogeneity: intermountain Journal of sciences, v. 5, p. 23–27.

Ritter, D. F., Kochel, R. C., Miller, J. R., & Miller, J. R., 2002. *Process geomorphology* (3rd ed., p. 546). Dubuque, Iowa: Wm. C. Brown.

Rogers, J., Smith, G.A., and Rowe, H., 1996, History of formation and drainage of Pleistocene lakes in the Valles caldera: New Mexico Geological Society, 47th Field Conference, Guidebook, p. 14-16. https://doi.org/10.56577/FFC-47

Rogers, J.B. and Smartt, R.A., 1996, Climatic influences on Quaternary alluvial stratigraphy and terrace formation in the Jemez River valley, New Mexico: New Mexico Geological Society, Guidebook 47

Rogers, J.B., 1996, The fluvial landscape evolution of San Diego Canyon, Jemez Mountains, New Mexico: Unpub. M.S. thesis, Albuquerque, University of New Mexico.

Schaen, A.J. et al., 2021, Interpreting and reporting 40Ar/39Ar geochronologic data: GSA Bulletin, v. 133, p. 461–487, doi:10.1130/B35560.1.

Schwanghart, W., and Scherler, D., 2014, Short Communication: TopoToolbox 2 – MATLAB-based software for topographic analysis and modeling in Earth surface sciences: Earth Surface Dynamics, v. 2, p. 1–7, doi:10.5194/esurf-2-1-2014.

Shaw, C.A., and Karlstrom, K.E., 1999, The Yavapai-Mazatzal crustal boundary in the Southern Rocky Mountains: Rocky Mountain Geology, v. 34, p. 37–52, doi:10.2113/34.1.37.

Sklar, L., and Dietrich, W.E., 1998, River longitudinal profiles and bedrock incision models: Stream power and the influence of sediment supply: Geophysical Monograph-American Geophysical Union, v. 107, p. 237–260.

Smith, G.A., and Lavine, A., 1996, What is the Cochiti Formation?: New Mexico Geological Society, 47th Field Conference, Guidebook, p.219-224. https://doi.org/10.56577/FFC-47.219

Snyder, N.P., Whipple, K.X., Tucker, G.E., and Merritts, D.J., 2000, Landscape response to tectonic forcing: Digital elevation model analysis of stream profiles in the Mendocino triple junction region, northern California: GSA Bulletin, v. 112, p. 1250–1263, doi:10.1130/0016-7606(2000)112<1250:LRTTFD>2.0.CO;2.

Strahler, A.N., 1952, Hypsometric (Area-Altitude) Analysis Of Erosional Topography: GSA Bulletin, v. 63, p. 1117–1142, doi:10.1130/0016-7606(1952)63[1117:HAAOET]2.0.CO;2.

Tafoya, A.J., 2012, Uranium-series geochronology and stable isotope analysis of travertine from Soda Dam, New Mexico: a Quaternary record of episodic spring discharge and river incision in the Jemez Mountains hydrothermal system, University of New Mexico Dissertations and Theses

Thompson Jobe, J.A., and Chupik, C., 2021, Low-Rate Faulting on the Margin of the Colorado Plateau and Rio Grande Rift in North-Central New Mexico: Tectonics, v. 40, p. e2021TC006860, doi:10.1029/2021TC006860.

Tucker, G.E., and Whipple, K.X., 2002, Topographic outcomes predicted by stream erosion models: Sensitivity analysis and intermodel comparison: TOPOGRAPHIC PREDICTIONS: Journal of Geophysical Research: Solid Earth, v. 107, p. ETG 1-1-ETG 1-16,

Turbeville, B. N., and S. Self (1988), San Diego Canyon ignimbrites: Pre-Bandelier tuff explosive rhyolitic volcanism in the Jemez Mountains, New Mexico, *J. Geophys. Res.*, 93(B6), 6148–6156, doi:10.1029/JB093iB06p06148.

U.S. Geological Survey and New Mexico Bureau of Mines and Mineral Resources, Quaternary fault and fold database for the United States, at: https://www.usgs.gov/natural-hazards/earthquake-hazards/faults.

U.S. Geological Survey, 2019, National Hydrography Dataset (ver. USGS National Hydrography Dataset Best Resolution (NHD) for Hydrologic Unit (HU) 4 - 2024 (published 20191002)), at: https://www.usgs.gov/national-hydrography/access-national-hydrography-products

Wegmann, K.W., and Pazzaglia, F.J., 2009, Late Quaternary fluvial terraces of the Romagna and Marche Apennines, Italy: Climatic, lithologic, and tectonic controls on terrace genesis in an active orogen: Quaternary Science Reviews, v. 28, p. 137–165, doi:10.1016/j.quascirev.2008.10.006.

Whipple, K.X., and Tucker, G.E., 1999, Dynamics of the stream-power river incision model: Implications for height limits of mountain ranges, landscape response timescales, and

research needs: Journal of Geophysical Research: Solid Earth, v. 104, p. 17661–17674, doi:10.1029/1999jb900120.

Whipple, K.X., and Tucker, G.E., 2002, Implications of sediment-flux-dependent river incision models for landscape evolution: Journal of Geophysical Research: Solid Earth, v. 107, p. ETG 3-1, doi:10.1029/2000JB000044.

Whittaker, A.C., Attal, M., Cowie, P.A., Tucker, G.E., and Roberts, G., 2008, Decoding temporal and spatial patterns of fault uplift using transient river long profiles: Geomorphology, v. 100, p. 506–526, doi:10.1016/j.geomorph.2008.01.018.

Willett, S.D., McCoy, S.W., Perron, J.T., Goren, L., and Chen, C.-Y., 2014, Dynamic Reorganization of River Basins: Science, v. 343, p. 1248765, doi:10.1126/science.1248765.

Wisniewski, P.A., and Pazzaglia, F.J., 2002, Epeirogenic Controls on Canadian River Incision and Landscape Evolution, Great Plains of Northeastern New Mexico: The Journal of Geology, v. 110, p. 437–456, doi:10.1086/340441.

Wobus, C., Whipple, K.X., Kirby, E., Snyder, N., Johnson, J., Spyropolou, K., Crosby, B., and Sheehan, D., 2006, Tectonics from topography: Procedures, promise, and pitfalls, *in* Willett, S.D., Hovius, N., Brandon, M.T., and Fisher, D.M. eds., Tectonics, Climate, and Landscape Evolution, Geological Society of America, v. 398, p. 0, doi:10.1130/2006.2398(04).

WoldeGabriel G., Naranjo A.P., Fittipaldo M.M., 2007, Distribution, geochemistry, and correlation of Pliocene tephra in the Pajarito Plateau, New Mexico Geological Society, 58th Field Conference, Guidebook, p. 275–283. https://doi.org/10.56577/FFC-58.275

Woodward, L. A., 1987, Geology and mineral resources of Sierra Nacimiento and vicinity, New Mexico, v. 42, New Mexico Bureau of Mines & Mineral Resources.

Woodward, L.A. and Reutschillang, 1976, Geology of the San Ysidro quadrangle, New Mexico: New Mexico Bureau of Mines and Mineral Resources, Geologic map 37, 1:24,000 scale.

APPENDIX

i. Notes for $^{39}Ar/^{40}Ar$ geochronology

Isotopic ratios corrected for blank, radioactive decay, and mass discrimination, not corrected for interfering reactions.
Errors quoted for individual analyses include analytical error only, without interfering reaction or J uncertainties.

Mean age is weighted mean age of Taylor (1982). Mean age error is weighted error of the mean (Taylor, 1982), multiplied by the root of the MSWD where MSWD>1, and also incorporates uncertainty in J factors and irradiation correction uncertainties.

Decay constants and isotopic abundances after Steiger and Jäger (1977).

symbol preceding sample ID denotes analyses excluded from mean age calculations.
Ages calculated relative to FC-2 Fish Canyon Tuff sanidine interlaboratory standard at 28.201 Ma

Decay Constant (LambdaK (total)) = 5.463e-10/a

Correction factors:

$(^{39}Ar/^{37}Ar)_{Ca} = 0.000724 \pm 0.000007$

$(^{36}Ar/^{37}Ar)_{Ca} = 0.0002758 \pm 0.0000014$

$(^{40}Ar/^{39}Ar)_{K} = 0.007401 \pm 0.00033$

ii. Summary DS Sample Locations and Ages

Sample	lat	long	MDA Age	MDA error 1σ	N	Comments
CR21-RS-01	35.542953	-106.843855	0.603	0.015	1	Dominated by mid-Tertiary and Mesozoic grains
CR21-RS-02	35.547639	-106.834462	20.5	0.3	1	Dominated by Mesozoic grains
CR21-RS-03b	35.547639	-106.834462	1.08	0.08	3	Dominated by mid-Tertiary and Mesozoic grains
CR21-RS-04	35.552638	-106.83824	1.164	0.01	1	~40 grains less than 4 Ma
C22-TA-1A	35.506556	-106.83581	32.49	0.17	4	Dominated by mid-Tertiary and Mesozoic grains
C22-TA-1B	35.506556	-106.83581	168.7	1.5	1	Dominated by Mesozoic grains
CR21-LdA1	35.24569	-106.86887	16.85	0.04	2	Dominated by mid-Tertiary and late Cenozoic grains

CR21-LdA2	35.24569	-106.86887	24.76	0.04	3	Dominated by mid-Tertiary and late Cenozoic grains
CR21-LdA3	35.24569	-106.86887	14.12	0.22	1	Dominated by mid-Tertiary and Cenozoic-Mesozoic grains
CR22-G1	35.672396	-106.75392	1.194	30.3	28	
CR22-G2	35.672396	-106.75392	0.544	10.7	17	
CR22-G3	35.672396	-106.75392	1.225	136	81	

iii. La Junta Qt1 Terrace Laser Data

ID	Power	$^{40}Ar/^{39}Ar$	$^{37}Ar/^{39}Ar$	$^{36}Ar/^{39}Ar$	$^{39}Ar_K$	K/Ca	$^{40}Ar^*$	Age	±1σ
	(watts)			(x 10^{-3})	(x 10^{-15} mol)		(%)	(Ma)	(Ma)
CR22-G1, Detrital Sanidine, J=0.001502±0.02%, IC=1.006065±0.0005497, NM-328A, Lab#=70506, Argus VI									
82	1.75	0.8308	0.0037	1.558	0.161	137.5	44.1	0.998	0.076
71	1.75	0.5330	0.0036	0.4071	0.428	141.5	77.2	1.115	0.025
68	1.75	0.4958	0.0067	0.2616	0.233	76.7	84.3	1.131	0.048
75	1.75	0.4804	0.0083	0.1803	0.566	61.2	88.9	1.155	0.018
77	1.75	0.4636	0.0072	0.1234	0.540	70.6	92.1	1.155	0.019
80	1.75	0.4578	0.0083	0.0933	0.446	61.4	94.0	1.164	0.023
78	1.75	0.5089	0.0096	0.2623	0.412	53.2	84.7	1.167	0.025
81	1.75	0.5947	0.0041	0.5476	0.426	124.0	72.5	1.170	0.029
51	1.75	0.4787	0.0084	0.1448	0.554	60.9	91.1	1.180	0.024
15	1.75	0.5010	0.0158	0.2153	0.306	32.2	87.4	1.185	0.043
76	1.75	0.4675	0.0093	0.0990	0.554	54.9	93.8	1.186	0.018
09	1.75	0.6471	0.0050	0.7049	0.462	102.2	67.5	1.187	0.038
79	1.75	0.5121	0.0075	0.2485	0.462	68.3	85.6	1.187	0.025
11	1.75	0.5276	0.0123	0.2939	0.301	41.6	83.5	1.194	0.047
07	1.75	0.4969	0.0108	0.1839	0.393	47.4	89.1	1.198	0.032
70	1.75	0.4997	0.0070	0.1911	0.379	73.1	88.6	1.199	0.032
03	1.75	0.4805	0.0161	0.1220	0.743	31.6	92.7	1.205	0.021
01	1.75	0.5095	0.0075	0.2164	0.534	68.2	87.4	1.206	0.027
14	1.75	0.4837	0.0131	0.1295	0.547	39.1	92.2	1.207	0.025
13	1.75	0.5012	0.0188	0.1754	0.738	27.2	89.8	1.219	0.020
69	1.75	0.6309	0.0080	0.5973	0.577	64.1	71.8	1.230	0.023
24	1.75	0.4861	0.0055	0.1044	0.628	92.6	93.6	1.232	0.023
06	1.75	0.5303	0.0065	0.2485	0.382	78.9	86.0	1.237	0.033

18	1.75	0.4859	0.0053	0.0971	0.814	96.5	94.1	1.237	0.017
25	1.75	0.5163	0.0181	0.1990	0.536	28.3	88.7	1.241	0.027
43	1.75	0.6852	0.0102	0.7683	0.344	50.1	66.6	1.241	0.044
02	1.75	0.5061	0.0070	0.1593	0.472	73.0	90.7	1.243	0.032
17	1.75	0.5318	0.0074	0.2443	0.343	69.3	86.3	1.244	0.037
65	1.75	0.5090	0.0109	0.1677	0.583	46.9	90.3	1.245	0.022
26	1.75	0.4925	0.0098	0.1074	0.560	51.9	93.6	1.248	0.026
38	1.75	0.4749	0.0071	0.0446	0.479	72.2	97.3	1.250	0.027
08	1.75	0.4944	0.0073	0.1076	0.524	69.6	93.6	1.253	0.025
05	1.75	0.5313	0.0136	0.2338	0.520	37.6	87.0	1.253	0.028
64	1.75	0.4752	0.0094	0.0422	0.959	54.3	97.5	1.254	0.014
58	1.75	0.4606	0.0098	-0.0155	0.357	52.0	101.2	1.260	0.033
45	1.75	0.5690	0.0066	0.3503	0.463	77.2	81.7	1.260	0.029
60	1.75	0.4827	0.0112	0.0585	0.802	45.7	96.6	1.261	0.016
63	1.75	0.4674	0.0088	0.0058	0.506	57.9	99.8	1.262	0.023
44	1.75	0.6120	0.0195	0.4938	0.448	26.2	76.1	1.265	0.039
21	1.75	0.5271	0.0111	0.1973	0.341	45.9	89.0	1.271	0.042
16	1.75	0.5865	0.0059	0.3953	0.447	86.6	79.9	1.272	0.030
61	1.75	0.4990	0.0069	0.0995	0.459	73.9	94.1	1.272	0.027
56	1.75	0.4899	0.0085	0.0681	0.475	60.2	96.0	1.273	0.026
34	1.75	0.4823	0.0093	0.0422	0.490	54.8	97.5	1.273	0.026
49	1.75	0.5457	0.0202	0.2570	0.500	25.3	86.2	1.275	0.028
37	1.75	0.4730	0.0138	0.0074	0.448	37.0	99.8	1.277	0.030
28	1.75	0.4911	0.0178	0.0688	0.373	28.7	96.1	1.278	
66	1.75	0.5784	0.0107	0.3612	0.497	47.7	81.5	1.278	0.028
19	1.75	0.5791	0.0169	0.3587	0.757	30.1	81.7	1.284	0.021
59	1.75	0.4779	0.0045	0.0074	0.319	112.8	99.6	1.288	0.041
32	1.75	0.4819	0.0078	0.0216	0.376	65.3	98.8	1.288	0.032
47	1.75	0.4826	0.0132	0.0246	0.738	38.6	98.7	1.289	0.019
67	1.75	0.5314	0.0254	0.1919	0.566	20.1	89.6	1.290	0.020
10	1.75	0.5039	0.0194	0.0915	0.533	26.3	94.9	1.295	0.030
40	1.75	0.5156	0.0088	0.1274	0.478	58.2	92.7	1.295	0.031
31	1.75	0.6462	0.0097	0.5654	0.257	52.7	74.0	1.299	0.053
52	1.75	0.4964	0.0074	0.0572	0.783	68.6	96.7	1.299	0.016
41	1.75	0.7802	0.0078	1.015	0.400	65.4	61.3	1.302	0.039
73	1.75	2.193	0.0137	5.796	0.347	37.2	21.7	1.303	0.059
55	1.75	0.5098	0.0091	0.0941	0.394	56.0	94.6	1.306	0.032
42	1.75	1.317	0.0157	2.829	0.396	32.6	36.3	1.307	0.046
57	1.75	0.4640	0.0098	-0.0685	0.426	52.0	104.6	1.313	0.027
20	1.75	0.4874	0.0066	0.0095	0.424	76.8	99.5	1.313	0.033
35	1.75	0.4809	0.0084	-0.0120	0.575	60.7	100.9	1.313	0.022

27	1.75	0.4994	0.0131	0.0462	0.472	38.9	97.4	1.318	0.027
39	1.75	0.5731	0.0130	0.2749	0.458	39.2	85.8	1.334	0.033
54	1.75	0.4917	0.0201	-0.0105	0.322	25.4	101.0	1.344	0.040
29	1.75	0.5144	0.0100	0.0534	0.329	51.0	97.0	1.352	0.039
62	1.75	0.5434	0.0077	0.1486	0.671	65.8	91.9	1.354	0.019
48	1.75	0.4868	0.0093	-0.0493	0.597	54.6	103.2	1.360	0.026
46	1.75	0.5604	0.0042	0.1737	0.337	122.2	90.8	1.380	0.045
36	1.75	0.5315	0.0089	0.0245	0.333	57.1	98.8	1.422	0.041
12	1.75	0.6325	0.0121	0.2130	0.448	42.1	90.1	1.548	0.030
23	1.75	1.027	0.0139	1.501	0.282	36.7	56.6	1.585	0.062
22	1.75	0.7237	0.0179	0.4476	0.327	28.5	81.7	1.609	0.044
30	1.75	0.6122	0.0204	0.0641	0.426	25.0	97.1	1.615	0.031
04	1.75	0.7223	0.0074	0.3962	0.485	69.2	83.7	1.645	0.035
53	1.75	0.6846	0.0127	0.2050	0.499	40.1	91.2	1.697	0.028
72	1.75	8.738	0.0078	0.0740	0.679	65.1	99.8	23.790	0.037
MDA ± 1σ			n=28	MSWD=2.05		68.8±30.3		1.194	0.007
CR22-G2, DetritalSanidine, J=0.0015006±0.02%, IC=1.006065±0.0005497, NM-328A, Lab#=70507, Argus VI									
23	1.75	0.3560	0.0267	0.7240	0.154	19.1	39.2	0.376	0.073
11	1.75	0.3461	0.0188	0.6183	0.297	27.2	46.5	0.433	0.041
13	1.75	0.3280	0.0160	0.5414	0.237	31.9	50.5	0.445	0.051
09	1.75	0.2927	0.0228	0.3767	0.270	22.4	61.6	0.483	0.044
65	1.75	0.4060	0.0155	0.7501	0.226	32.9	44.7	0.489	0.054
62	1.75	0.3344	0.0159	0.4632	0.377	32.0	58.5	0.526	0.034
56	1.75	0.2682	0.0167	0.2274	0.314	30.5	74.8	0.535	0.037
27	1.75	0.3101	0.0312	0.3428	0.231	16.4	67.4	0.560	0.055
92	1.75	0.3685	0.0163	0.5294	0.265	31.2	57.1	0.566	0.049
18	1.75	0.6635	0.0091	1.505	0.284	55.9	32.3	0.583	0.056
57	1.75	0.2909	0.0199	0.2453	0.275	25.7	75.0	0.584	0.043
31	1.75	0.2757	0.0356	0.1976	0.285	14.3	79.3	0.584	0.043
53	1.75	0.4670	0.0283	0.8382	0.219	18.1	46.6	0.588	0.052
43	1.75	0.3681	0.0243	0.4954	0.221	21.0	60.0	0.594	0.062
73	1.75	0.2926	0.0297	0.2233	0.258	17.2	77.7	0.609	0.047
86	1.75	0.4071	0.0114	0.6035	0.338	44.6	55.6	0.610	0.034
50	1.75	0.3251	0.0211	0.3268	0.197	24.2	70.1	0.612	0.062
49	1.75	0.3382	0.0324	0.3524	0.253	15.7	69.3	0.630	0.050
75	1.75	0.3224	0.0159	0.2938	0.405	32.1	72.9	0.630	0.030
72	1.75	0.3503	0.0196	0.3854	0.272	26.0	67.2	0.633	0.045
67	1.75	0.2735	0.0170	0.0950	0.283	30.0	90.0	0.657	0.042
35	1.75	0.3357	0.0290	0.3020	0.330	17.6	73.5	0.663	0.034

83	1.75	0.3367	0.0102	0.2928	0.365	50.1	74.0	0.669	0.031
95	1.75	0.4752	0.0232	0.7523	0.203	21.9	52.9	0.679	0.063
39	1.75	0.2853	0.0216	0.1087	0.429	23.6	89.1	0.680	0.027
30	1.75	0.3317	0.0354	0.2522	0.267	14.4	77.9	0.694	0.046
59	1.75	0.3265	0.0199	0.2296	0.487	25.6	79.2	0.694	0.028
76	1.75	0.5350	0.0157	0.7959	0.271	32.4	55.7	0.806	0.042
10	1.75	0.5303	0.0116	0.4874	0.316	44.1	72.6	1.043	0.037
07	1.75	0.6326	0.0053	0.7913	0.380	96.1	62.7	1.076	0.035
24	1.75	0.5896	0.0098	0.6343	0.208	52.2	67.9	1.086	0.061
12	1.75	0.6719	0.0061	0.9060	0.218	83.7	59.8	1.091	0.056
97	1.75	0.8097	0.0087	1.369	0.219	58.4	49.7	1.095	0.069
33	1.75	0.7274	0.0116	1.086	0.191	44.1	55.6	1.099	0.071
05	1.75	0.5496	0.0066	0.4684	0.318	77.1	74.6	1.110	0.037
03	1.75	0.7283	0.0179	1.062	0.206	28.5	56.7	1.122	0.062
55	1.75	0.5278	0.0110	0.3706	0.200	46.2	79.1	1.131	0.060
47	1.75	0.4922	0.0090	0.2480	0.222	56.5	85.0	1.132	0.059
16	1.75	0.4721	0.0147	0.1765	0.403	34.7	89.0	1.136	0.028
22	1.75	0.5328	0.0168	0.3816	0.163	30.3	78.8	1.137	0.070
21	1.75	1.018	0.0082	2.011	0.450	62.5	41.3	1.145	0.035
98	1.75	0.7788	0.0179	1.203	0.186	28.5	54.1	1.146	0.069
14	1.75	0.7177	0.0108	0.9914	0.218	47.5	58.9	1.148	0.052
34	1.75	0.5771	0.0101	0.5129	0.219	50.4	73.5	1.150	0.051
45	1.75	0.6413	0.0101	0.7184	0.177	50.7	66.6	1.160	0.078
06	1.75	0.8521	0.0066	1.423	0.243	77.4	50.3	1.167	0.061
37	1.75	0.4952	0.0089	0.2102	0.211	57.2	87.5	1.172	0.052
17	1.75	0.4820	0.0144	0.1653	0.285	35.3	90.0	1.172	0.042
32	1.75	0.5258	0.0128	0.3003	0.307	39.9	83.1	1.183	0.041
15	1.75	0.5900	0.0089	0.5152	0.238	57.3	74.0	1.183	0.056
66	1.75	0.6174	0.0116	0.6045	0.251	44.2	70.9	1.187	0.049
20	1.75	1.480	0.0185	3.525	0.202	27.6	29.4	1.188	0.087
25	1.75	0.8259	0.0125	1.307	0.252	40.7	52.9	1.190	0.053
28	1.75	0.5810	0.0083	0.4716	0.312	61.5	75.8	1.194	0.042
26	1.75	0.6832	0.0068	0.8141	0.343	74.6	64.5	1.197	0.041
61	1.75	0.4876	0.0258	0.1556	0.372	19.8	90.9	1.198	0.030
38	1.75	0.4654	0.0105	0.0684	0.306	48.5	95.8	1.204	0.038
69	1.75	0.4766	0.0223	0.1053	0.282	22.9	93.8	1.208	0.043
36	1.75	0.5715	0.0062	0.4076	0.345	81.7	78.7	1.220	0.036
54	1.75	0.5123	0.0090	0.1888	0.242	56.4	89.1	1.235	0.048
01	1.75	0.5575	0.0097	0.3367	0.443	52.5	82.1	1.240	0.029
81	1.75	0.5356	0.0022	0.2481	0.222	230.9	86.2	1.250	0.049
82	1.75	0.5484	0.0008	0.2853	0.329	654.8	84.4	1.254	0.035

96	1.75	0.6704	0.0161	0.6948	0.269	31.6	69.2	1.260	0.047
40	1.75	0.5091	0.0064	0.1459	0.297	79.3	91.5	1.261	0.037
68	1.75	0.4776	0.0118	0.0387	0.270	43.4	97.8	1.262	0.045
87	1.75	0.5607	0.0111	0.3104	0.379	46.0	83.6	1.270	0.033
29	1.75	0.5787	0.0106	0.3679	0.314	48.1	81.1	1.272	0.038
41	1.75	0.6512	0.0206	0.6149	0.302	24.8	72.0	1.273	0.045
94	1.75	0.5031	0.0116	0.1027	0.456	43.8	94.1	1.280	0.025
79	1.75	0.5508	0.0088	0.2557	0.256	58.2	86.2	1.287	0.049
88	1.75	0.8335	0.0109	1.206	0.229	46.6	57.0	1.292	0.057
70	1.75	0.5758	0.0169	0.3121	0.225	30.2	84.0	1.311	0.054
91	1.75	0.7155	0.0117	0.7703	0.437	43.6	68.0	1.322	0.028
85	1.75	0.5548	0.0170	0.2164	0.198	30.0	88.6	1.331	0.057
78	1.75	0.6352	0.0086	0.4354	0.303	59.5	79.6	1.373	0.041
84	1.75	0.6440	0.0041	0.4315	0.217	124.1	80.0	1.399	0.056
44	1.75	0.8059	0.0155	0.9779	0.255	32.9	64.0	1.402	0.056
99	1.75	0.6520	0.0079	0.4061	0.278	64.9	81.5	1.442	0.044
48	1.75	0.6255	0.0213	0.2659	0.186	23.9	87.6	1.486	0.066
46	1.75	1.156	0.0128	2.033	0.380	39.9	47.8	1.506	0.044
63	1.75	0.7556	0.0195	0.6530	0.258	26.1	74.4	1.529	0.046
80	1.75	0.6784	0.0200	0.3513	0.252	25.5	84.8	1.562	0.049
02	1.75	0.6488	0.0126	0.2438	0.253	40.3	88.9	1.566	0.048
74	1.75	0.6404	0.0223	0.2104	0.214	22.9	90.5	1.572	0.053
52	1.75	0.6146	0.0109	0.1167	0.246	46.8	94.5	1.575	0.042
MDA ± 1σ			n=17	MSWD=1.9 1		27.3 ±10.7		0.544	0.015
CR22-G3, Detrital Sanidine, J=0.0015457±0.02%, IC=1.006065±0.0005497, NM-328M, Lab#=70617, Argus VI									
102	1.75	0.5246	0.0116	0.4662	0.280	44.1	73.5	1.076	0.039
74	1.75	0.4689	0.0211	0.2620	0.081	24.1	83.6	1.09	0.13
78	1.75	0.4745	0.0041	0.2742	0.316	124.7	82.7	1.093	0.032
27	1.75	0.9555	0.0044	1.876	0.225	116.9	41.6	1.115	0.068
29	1.75	0.4621	0.0109	0.1874	0.262	46.7	88.0	1.132	0.047
17	1.75	0.5499	0.0093	0.4807	0.323	54.7	74.0	1.135	0.037
75	1.75	0.4614	0.0004	0.1784	0.239	1200.8	88.4	1.135	0.047
77	1.75	0.4777	0.0116	0.2265	0.351	44.2	86.0	1.144	0.032
19	1.75	0.4930	0.0091	0.2688	0.351	55.9	83.8	1.151	0.034
73	1.75	0.4975	0.0033	0.2775	0.249	155.0	83.3	1.155	0.042
68	1.75	0.4653	0.0114	0.1625	0.395	44.8	89.7	1.162	0.030
106	1.75	0.5479	0.0059	0.4366	0.270	87.0	76.2	1.165	0.040
104	1.75	0.4801	0.0102	0.2025	0.413	50.1	87.5	1.170	0.029
39	1.75	0.4563	0.0066	0.1185	0.377	77.6	92.3	1.172	0.030

23	1.75	0.4491	0.0043	0.0885	0.341	117.7	94.1	1.176	0.036
67	1.75	0.4965	0.0118	0.2469	0.267	43.3	85.3	1.180	0.044
33	1.75	0.5864	0.0106	0.5502	0.226	48.1	72.1	1.180	0.051
108	1.75	0.5302	0.0128	0.3594	0.176	39.8	79.9	1.181	0.063
35	1.75	0.4929	0.0180	0.2316	0.561	28.4	86.2	1.184	0.020
71	1.75	0.4655	0.0067	0.1312	0.441	76.7	91.6	1.187	0.027
56	1.75	0.4616	0.0116	0.1154	0.248	43.9	92.7	1.191	0.048
101	1.75	0.4566	0.0052	0.0936	0.278	97.8	93.9	1.193	0.041
97	1.75	0.4536	0.0066	0.0773	0.391	76.9	95.0	1.199	0.030
66	1.75	0.4426	0.0101	0.0396	0.292	50.4	97.5	1.200	0.037
65	1.75	0.4533	0.0090	0.0739	0.351	56.4	95.3	1.201	0.033
62	1.75	0.4700	0.0047	0.1191	0.305	107.6	92.5	1.210	0.035
15	1.75	0.4710	0.0102	0.1241	0.341	50.0	92.3	1.210	0.032
60	1.75	0.5850	0.0110	0.5088	0.150	46.3	74.1	1.210	0.078
31	1.75	0.4623	0.0013	0.0899	0.255	403.6	94.2	1.212	0.043
43	1.75	0.4638	0.0149	0.0977	0.189	34.2	93.9	1.213	0.057
13	1.75	0.4608	0.0046	0.0799	0.394	110.3	94.9	1.217	0.028
70	1.75	0.4553	0.0071	0.0618	0.367	72.0	96.1	1.217	0.031
14	1.75	0.4776	0.0084	0.1375	0.388	61.0	91.5	1.217	0.029
32	1.75	0.4726	0.0160	0.1206	0.542	31.9	92.6	1.218	0.022
83	1.75	0.4432	0.0100	0.0193	0.442	51.0	98.9	1.219	0.022
96	1.75	0.4712	0.0055	0.1130	0.203	92.0	92.9	1.219	0.055
64	1.75	0.6115	0.0095	0.5886	0.583	53.9	71.3	1.219	0.025
100	1.75	0.4599	0.0083	0.0707	0.317	61.7	95.5	1.223	0.034
42	1.75	0.4720	0.0125	0.1123	0.470	41.0	93.1	1.223	0.026
40	1.75	0.4861	0.0020	0.1540	0.270	249.1	90.5	1.226	0.040
30	1.75	0.4793	0.0063	0.1321	0.684	81.6	91.8	1.226	0.019
107	1.75	0.4852	0.0154	0.1534	0.381	33.1	90.8	1.227	0.030
20	1.75	0.5592	0.0217	0.4000	0.401	23.6	78.9	1.232	0.030
18	1.75	0.4775	0.0047	0.1185	0.397	108.9	92.6	1.232	0.028
63	1.75	0.5195	0.0194	0.2625	0.291	26.3	85.2	1.234	0.036
82	1.75	0.5061	0.0187	0.2100	0.247	27.2	87.9	1.239	0.043
03	1.75	0.5115	0.0138	0.2265	0.389	36.9	86.9	1.240	0.030
87	1.75	0.4723	0.0088	0.0909	0.504	58.0	94.4	1.241	0.021
72	1.75	0.4816	0.0139	0.1237	0.391	36.7	92.5	1.241	0.030
09	1.75	0.5014	0.0114	0.1871	0.420	44.9	89.0	1.243	0.029
53	1.75	0.5470	0.0034	0.3385	0.488	149.6	81.5	1.244	0.026
47	1.75	0.4991	0.0303	0.1821	0.199	16.8	89.6	1.246	0.058
48	1.75	0.4487	0.0643	0.0183	0.173	7.9	99.9	1.247	0.066
103	1.75	0.5526	0.0117	0.3524	0.147	43.7	81.1	1.250	0.074
79	1.75	0.4796	0.0059	0.1011	0.543	85.9	93.8	1.252	0.019

90	1.75	0.4586	0.0095	0.0263	0.467	53.6	98.4	1.256	0.022
80	1.75	0.5725	0.0090	0.4114	0.216	56.6	78.6	1.256	0.046
61	1.75	0.4515	0.0087	0.0018	0.371	58.7	100.0	1.257	0.028
11	1.75	0.4690	0.0077	0.0598	0.791	66.0	96.3	1.257	0.017
109	1.75	0.4729	0.0068	0.0680	0.289	74.9	95.8	1.262	0.041
88	1.75	0.4625	0.0089	0.0326	0.324	57.5	98.0	1.262	0.034
21	1.75	0.4957	0.0127	0.1458	0.469	40.1	91.4	1.262	0.027
38	1.75	0.4339	0.0079	-0.0650	0.207	64.6	104.6	1.262	0.057
95	1.75	0.4533	0.0112	0.0004	0.505	45.6	100.2	1.263	0.023
69	1.75	0.5252	0.0151	0.2443	0.168	33.9	86.3	1.264	0.065
45	1.75	0.4565	0.0143	0.0113	0.633	35.6	99.5	1.264	0.020
55	1.75	0.6023	0.0087	0.5016	0.215	58.5	75.2	1.265	0.053
05	1.75	0.6653	0.0204	0.7171	0.246	25.0	68.0	1.266	0.055
50	1.75	0.6928	0.0050	0.7941	0.151	101.3	65.8	1.276	0.080
41	1.75	0.4388	0.0156	-0.0655	0.228	32.6	104.8	1.278	0.052
84	1.75	0.4537	0.0061	-0.0204	0.191	84.0	101.4	1.281	0.053
22	1.75	0.4888	0.0223	0.1013	0.234	22.9	94.1	1.282	0.049
16	1.75	0.5441	0.0043	0.2829	0.479	117.5	84.5	1.283	0.027
06	1.75	0.4655	0.0083	0.0085	0.367	61.5	99.6	1.290	0.034
93	1.75	0.4615	0.0092	-0.0070	0.323	55.5	100.6	1.292	0.035
86	1.75	0.4875	0.0053	0.0774	0.103	95.4	95.3	1.29	0.10
105	1.75	0.4863	0.0100	0.0721	0.192	50.8	95.7	1.296	0.056
37	1.75	0.4980	0.0073	0.1095	0.290	70.0	93.5	1.298	0.042
10	1.75	0.4691	0.0116	0.0112	0.308	44.0	99.5	1.299	0.039
81	1.75	0.4551	0.0065	-0.0375	0.255	78.1	102.6	1.299	0.040
44	1.75	0.4700	0.0160	0.0128	0.291	31.9	99.5	1.301	0.038
110	1.75	0.6376	0.0055	0.5636	0.275	92.0	73.6	1.313	0.045
91	1.75	0.4780	0.0089	0.0217	0.434	57.1	98.8	1.315	0.024
94	1.75	0.4607	0.0066	-0.0386	0.398	77.1	102.6	1.316	0.028
89	1.75	0.4690	0.0018	-0.0454	0.200	279.0	102.9	1.344	0.054
85	1.75	0.4714	0.0106	-0.0400	0.195	48.2	102.7	1.348	0.056
54	1.75	0.5246	0.0071	0.1307	0.234	71.7	92.6	1.355	0.048
99	1.75	0.5169	0.0078	0.0672	0.231	65.8	96.2	1.387	0.048
98	1.75	0.5060	0.0242	0.0006	0.204	21.0	100.4	1.415	0.052
58	1.75	0.6445	0.0178	0.4304	0.426	28.7	80.3	1.446	0.027
59	1.75	0.4430	0.0227	-0.2627	0.100	22.5	118.2	1.46	0.12
76	1.75	0.6074	0.0283	0.2685	0.326	18.1	87.2	1.479	0.035
02	1.75	0.5794	0.0173	0.1470	0.867	29.6	92.6	1.499	0.014
28	1.75	0.5926	0.0106	0.1104	0.243	48.3	94.6	1.565	0.048
92	1.75	1.169	0.0090	2.033	0.043	56.4	48.3	1.59	0.29
07	1.75	0.6069	0.0144	0.1281	0.593	35.5	93.9	1.592	0.020

49	1.75	0.5779	0.0140	0.0248	0.258	36.4	98.9	1.596	0.048
04	1.75	0.7012	0.0141	0.4300	0.539	36.3	81.8	1.606	0.024
08	1.75	0.8818	0.0130	0.9976	0.180	39.1	66.4	1.642	0.072
36	1.75	0.6373	0.0215	0.1368	0.255	23.7	93.9	1.672	0.047
57	1.75	0.6777	0.0232	0.1189	0.400	22.0	95.0	1.802	0.029
46	1.75	1.195	0.0598	0.3999	0.187	8.5	90.5	3.038	0.061
51	1.75	1.646	0.0150	0.8634	0.315	34.0	84.5	3.915	0.040
25	1.75	1.460	0.0078	0.1303	0.346	65.2	97.4	3.997	0.036
26	1.75	3.869	0.0259	0.2413	0.287	19.7	98.2	10.700	0.059
52	1.75	6.570	0.0196	0.2854	0.235	26.0	98.7	18.242	0.088
34	1.75	150.5	0.0008	9.076	1.221	621.3	98.2	376.76	0.95
12	1.75	417.9	0.0038	0.3194	0.513	134.4	100.0	912.0	3.7
01	1.75	420.8	0.0140	1.038	0.395	36.4	99.9	916.5	3.8
MDA age ± 1σ			n=81	MSWD=1.85		81±136		1.225	0.005

iv. Tierra Amarilla Anticline Surface Age-Spectrum

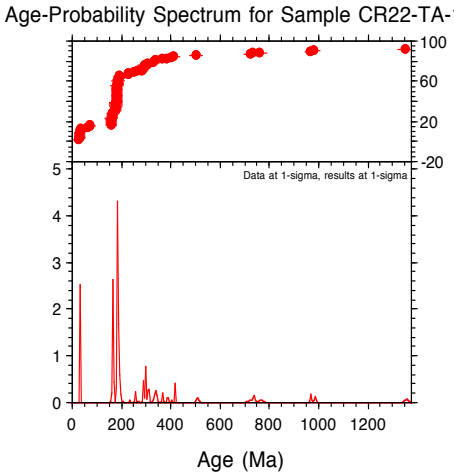

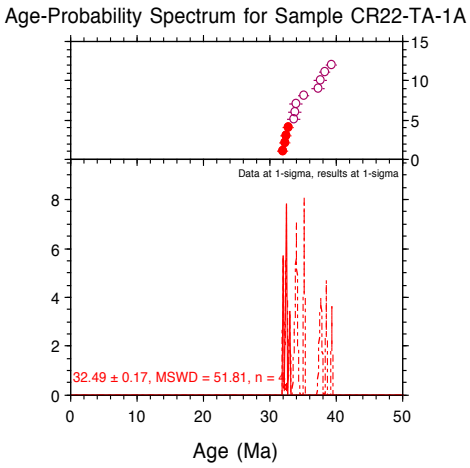

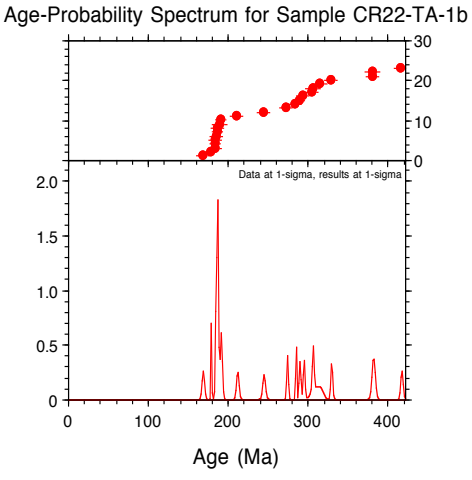

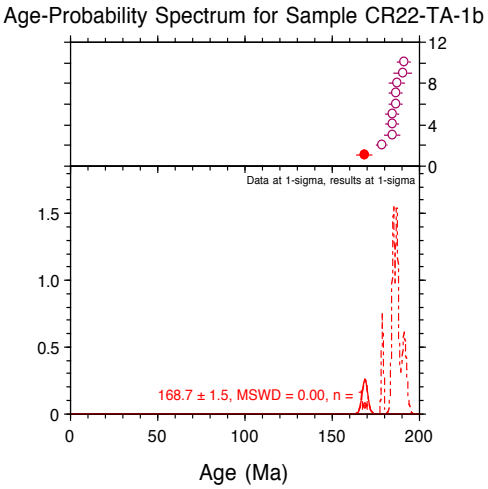

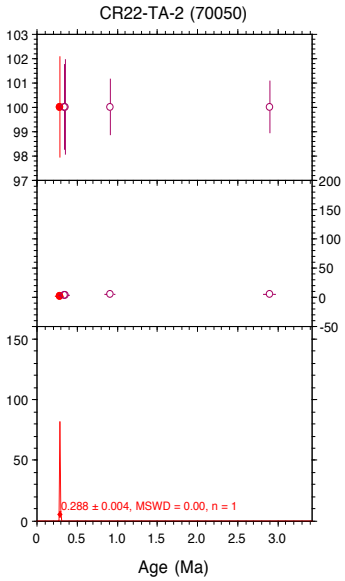

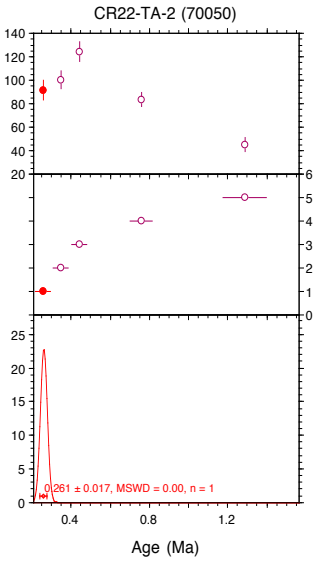

v. *Río Guadalupe/Jemez Confluence Age-Spectrum*

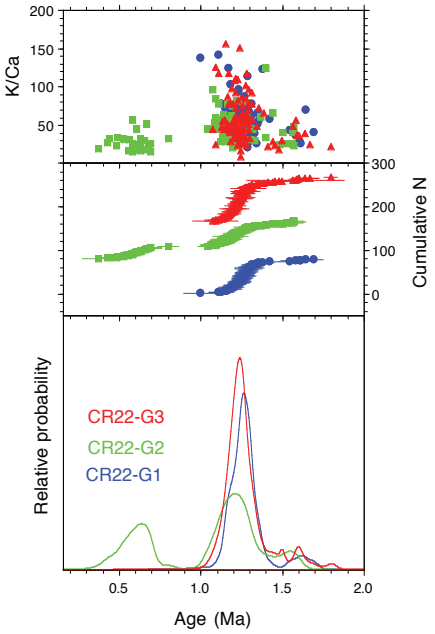

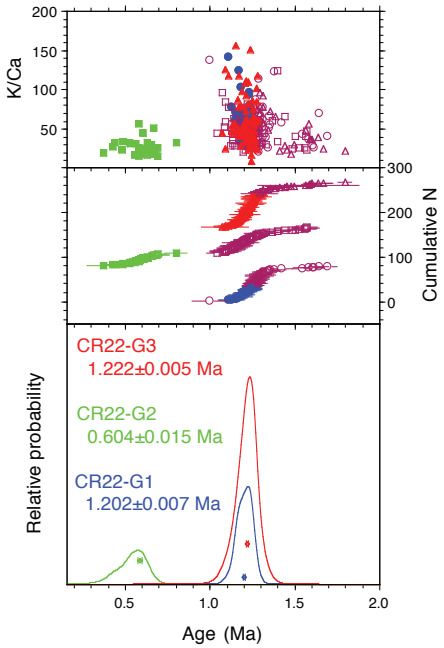

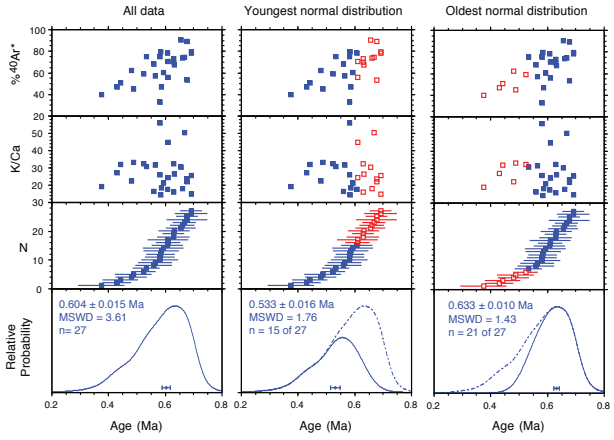

vi. Soda Dam Clast
Results and Data

Summary of
$^{40}Ar/^{39}Ar$ results

					Mean Age								
Sample	Lat, Long	L#	Irrad	min	analysis	n	MSWD	K/Ca	±	1σ	**Age(Ma)**	±	**1σ**
BR21-SD-1b	35.788913, -106.69122	70964	NM-333A	Sanidine	Mean	13	2.6	24.5	±	7.2	**1.217**	±	**0.005**
BR21-SD-1c	35.788913, -106.69122	70967	NM-333A	Sanidine	Mean	12	5.9	24.5	±	8.7	**1.210**	±	**0.007**
BR23-SD-1a	35.788913, -106.69122	70954	NM-333A	Sanidine	Mean	13	4.0	24.7	±	7.3	**1.207**	±	**0.005**
BR23-SD-1b	35.788913, -106.69122	70956	NM-333A	Sanidine	Mean	14	2.3	34.5	±	13.9	**1.225**	±	**0.003**
BR23-SD-1c	35.788913, -106.69122	70958	NM-333A	Sanidine	Mean	13	10.6	28.5	±	11.1	**1.233**	±	**0.007**
BR23-SD-2a	35.788786, -106.69181	70960	NM-333A	Sanidine	Mean	15	2.3	25.5	±	7.2	**1.212**	±	**0.004**
BR23-SD-2b	35.788786, -106.69181	70962	NM-333A	Sanidine	Mean	15	3.5	33.7	±	7.9	**1.228**	±	**0.004**
BR23-SD-3c	35.788786, -106.69181	70963	NM-333A	Sanidine	Mean	14	3.7	23.1	±	10.2	**1.215**	±	**0.005**

ID	Power	40Ar/39Ar	37Ar/39Ar	36Ar/39Ar	39ArK	K/Ca	40Ar*	Age	±1σ
	(watts)			(x 10^{-3})	(x 10^{-15} mol)		(%)	(Ma)	(Ma)
BR21-SD-1b, Sanidine, J=0.0004259±0.04%, IC=1.00376±0.0006249, NM-333A, Lab#=70964, Argus VI									
13	1.75	9.949	0.0193	28.55	1.422	26.4	15.2	1.174	0.021
11	1.75	8.490	0.0255	23.59	1.288	20.0	17.8	1.180	0.020
07	1.75	2.874	0.0351	4.582	0.628	14.5	52.9	1.181	0.013
02	1.75	4.552	0.0373	10.23	1.348	13.7	33.5	1.187	0.013
10	1.75	2.969	0.0267	4.768	1.448	19.1	52.5	1.211	0.009
12	1.75	3.184	0.0138	5.482	1.283	37.1	49.0	1.214	0.010
04	1.75	4.833	0.0248	11.03	1.273	20.6	32.5	1.221	0.015
05	1.75	2.207	0.0147	2.141	0.877	34.8	71.3	1.222	0.010
01	1.75	2.014	0.0219	1.490	1.073	23.3	78.1	1.222	0.007
09	1.75	2.065	0.0162	1.634	0.744	31.5	76.6	1.228	0.009
03	1.75	2.233	0.0186	2.198	1.355	27.5	70.9	1.229	0.007
14	1.75	4.549	0.0225	10.03	1.447	22.6	34.8	1.231	0.013
08	1.75	6.087	0.0189	15.15	1.250	27.0	26.4	1.251	0.017
15	1.75	2.571	0.0229	3.152	1.047	22.3	63.7	1.273	0.008
06	1.75	3.408	0.0152	5.602	1.795	33.6	51.3	1.361	0.010
Mean age ± 1σ			n=13	MSWD=2.64		24.5 ± 7.2		1.217	0.005
BR21-SD-1c, Sanidine, J=0.0004263±0.04%, IC=1.00376±0.0006249, NM-333A, Lab#=70967, Argus VI									
06	1.75	3.562	0.0406	7.044	0.774	12.6	41.5	1.151	0.015
12	1.75	5.374	0.0585	13.11	0.383	8.7	27.9	1.167	0.029
02	1.75	3.177	0.0192	5.605	1.193	26.6	47.8	1.182	0.010
01	1.75	3.346	0.0213	6.155	1.125	23.9	45.6	1.187	0.012
07	1.75	1.659	0.0175	0.3995	0.643	29.2	92.9	1.197	0.008
08	1.75	1.746	0.0172	0.6855	0.891	29.6	88.4	1.199	0.007
14	1.75	2.744	0.0347	4.056	0.460	14.7	56.3	1.202	0.019
05	1.75	5.648	0.0194	13.87	2.152	26.3	27.3	1.203	0.013
13	1.75	2.028	0.0146	1.547	0.662	34.9	77.4	1.220	0.010
10	1.75	1.734	0.0149	0.5475	0.243	34.1	90.7	1.221	0.019
03	1.75	1.770	0.0156	0.6509	1.119	32.7	89.2	1.226	0.006
11	1.75	2.028	0.0254	1.429	0.849	20.1	79.2	1.248	0.008
04	1.75	2.257	0.0181	1.808	0.834	28.1	76.3	1.339	0.008
09	1.75	2.315	0.0263	1.816	0.784	19.4	76.8	1.383	0.009
Mean age ± 1σ			n=12	MSWD=5.89		24.5 ± 8.7		1.210	0.007
BR23-SD-1a, Sanidine, J=0.0004242±0.03%, IC=1.00376±0.0006249, NM-333A, Lab#=70954, Argus VI									

05	1.75	4.686	0.0160	10.76	0.723	31.8	32.0	1.163	0.019
02	1.75	3.897	0.0288	8.067	0.832	17.7	38.8	1.170	0.014
07	1.75	2.171	0.0168	2.199	0.626	30.3	70.0	1.176	0.011
03	1.75	2.145	0.0186	2.064	0.816	27.4	71.5	1.187	0.009
12	1.75	1.719	0.0442	0.5953	0.638	11.5	89.9	1.195	0.008
15	1.75	1.861	0.0316	1.059	0.648	16.1	83.2	1.197	0.009
11	1.75	1.998	0.0243	1.518	0.894	21.0	77.6	1.198	0.008
13	1.75	2.752	0.0136	4.048	0.452	37.4	56.5	1.202	0.018
09	1.75	2.013	0.0275	1.522	0.809	18.6	77.7	1.209	0.009
10	1.75	2.488	0.0188	3.122	1.407	27.1	62.9	1.210	0.007
08	1.75	2.575	0.0218	3.398	1.385	23.4	61.0	1.214	0.007
14	1.75	1.820	0.0170	0.8091	1.910	30.0	86.9	1.222	0.004
04	1.75	5.567	0.0179	13.46	1.719	28.5	28.5	1.229	0.015
01	1.75	4.852	0.0208	10.86	1.549	24.5	33.8	1.270	0.007
06	1.75	15.64	0.0193	47.09	1.615	26.4	11.0	1.333	0.026
Mean age ± 1σ			n=13	MSWD=4.01		24.7 ± 7.3		1.207	0.005

BR23-SD-1b, Sanidine, J=0.0004229±0.02%, IC=1.00376±0.0006249, NM-333A, Lab#=70956, Argus VI

06	1.75	1.865	0.0176	1.061	0.538	29.0	83.2	1.195	0.010
10	1.75	3.797	0.0223	7.557	1.462	22.9	41.1	1.205	0.011
14	1.75	1.923	0.0136	1.192	0.554	37.6	81.7	1.210	0.010
09	1.75	1.817	0.0391	0.8077	1.001	13.0	87.0	1.218	0.006
03	1.75	2.446	0.0074	2.911	0.806	68.7	64.7	1.221	0.010
11	1.75	2.243	0.0153	2.226	0.343	33.3	70.6	1.222	0.016
05	1.75	1.871	0.0171	0.9644	0.967	29.9	84.8	1.222	0.006
13	1.75	1.944	0.0114	1.206	1.064	44.7	81.6	1.223	0.007
07	1.75	1.778	0.0197	0.6463	1.343	25.9	89.3	1.224	0.004
01	1.75	1.901	0.0177	1.053	1.191	28.8	83.6	1.226	0.005
15	1.75	1.737	0.0152	0.4785	0.626	33.5	91.9	1.230	0.008
12	1.75	1.863	0.0093	0.8654	0.803	55.1	86.3	1.238	0.007
08	1.75	1.891	0.0157	0.9496	1.083	32.4	85.2	1.241	0.006
02	1.75	4.093	0.0185	8.400	0.553	27.5	39.3	1.242	0.019
04	1.75	1.828	0.0226	0.2844	0.653	22.6	95.5	1.345	0.007
Mean age ± 1σ			n=14	MSWD=2.26		34.5 ± 13.9		1.225	0.003

BR23-SD-1c, Sanidine, J=0.0004225±0.03%, IC=1.00376±0.0006249, NM-333A, Lab#=70958, Argus VI

11	1.75	1.817	0.0179	0.9202	0.656	28.4	85.1	1.190	0.008
07	1.75	1.906	0.0178	1.155	0.883	28.7	82.1	1.204	0.006
14	1.75	1.945	0.0174	1.253	0.554	29.4	81.0	1.212	0.011
06	1.75	2.165	0.0094	1.982	1.040	54.1	72.9	1.215	0.008

01	1.75	2.756	0.0208	3.969	0.954	24.6	57.4	1.219	0.011
05	1.75	1.918	0.0158	1.129	0.836	32.2	82.6	1.220	0.007
10	1.75	2.689	0.0172	3.705	0.898	29.7	59.2	1.228	0.010
08	1.75	4.520	0.0361	9.859	0.255	14.1	35.5	1.238	0.031
15	1.75	1.882	0.0165	0.8974	1.367	31.0	85.9	1.245	0.005
03	1.75	2.235	0.0145	2.043	1.709	35.1	72.9	1.256	0.006
13	1.75	2.849	0.0237	4.116	0.733	21.6	57.3	1.258	0.012
02	1.75	2.943	0.0688	4.416	1.115	7.4	55.7	1.265	0.011
09	1.75	1.831	0.0149	0.5445	0.521	34.3	91.2	1.286	0.010
04	1.75	1.852	0.0209	0.3822	0.939	24.4	94.0	1.340	0.005
12	1.75	3.464	0.0434	5.735	0.579	11.7	51.1	1.364	0.017
Mean age ± 1σ			n=13	MSWD=10.57		28.5 ± 11.1		1.233	0.007

BR23-SD-2a, Sanidine, J=0.0004232±0.03%, IC=1.00376±0.0006249, NM-333A, Lab#=70960, Argus VI

06	1.75	15.15	0.0201	46.16	1.460	25.4	9.9	1.160	0.025
07	1.75	3.341	0.0166	6.057	1.520	30.7	46.3	1.196	0.010
03	1.75	1.986	0.0364	1.465	1.119	14.0	78.3	1.199	0.006
01	1.75	2.945	0.0191	4.702	1.102	26.6	52.7	1.200	0.010
04	1.75	5.024	0.0158	11.72	1.666	32.3	31.0	1.205	0.013
11	1.75	1.903	0.0171	1.135	0.776	29.8	82.4	1.209	0.008
08	1.75	4.632	0.0199	10.35	0.877	25.7	33.9	1.213	0.017
09	1.75	1.820	0.0173	0.8300	0.671	29.5	86.5	1.214	0.008
14	1.75	1.944	0.0364	1.255	0.720	14.0	81.0	1.214	0.009
13	1.75	4.473	0.0158	9.793	1.277	32.4	35.2	1.218	0.013
02	1.75	2.243	0.0149	2.241	0.761	34.2	70.4	1.219	0.010
15	1.75	7.776	0.0202	20.93	0.580	25.3	20.4	1.227	0.029
05	1.75	2.331	0.0411	2.468	1.072	12.4	68.8	1.237	0.009
10	1.75	3.601	0.0266	6.760	1.393	19.2	44.5	1.238	0.010
12	1.75	8.272	0.0166	22.51	1.066	30.7	19.5	1.250	0.025
Mean age ± 1σ			n=15	MSWD=2.27		25.5 ± 7.2		1.212	0.004

BR23-SD-2b, Sanidine, J=0.0004246±0.03%, IC=1.00376±0.0006249, NM-333A, Lab#=70962, Argus VI

15	1.75	1.751	0.0139	0.7944	0.339	36.6	86.6	1.173	0.015
11	1.75	2.342	0.0129	2.728	0.514	39.5	65.5	1.188	0.013
04	1.75	1.743	0.0189	0.6167	0.572	26.9	89.6	1.208	0.009
02	1.75	1.783	0.0172	0.7337	0.453	29.7	87.9	1.212	0.011
03	1.75	1.728	0.0110	0.5351	0.534	46.4	90.9	1.215	0.009
07	1.75	2.094	0.0183	1.760	0.590	27.9	75.1	1.218	0.011
12	1.75	2.550	0.0124	3.280	0.567	41.3	61.9	1.223	0.013
14	1.75	3.324	0.0147	5.897	0.243	34.7	47.5	1.224	0.028

08	1.75	2.936	0.0208	4.576	0.695	24.5	53.9	1.226	0.013
05	1.75	1.745	0.0131	0.5357	1.748	38.9	90.9	1.228	0.003
13	1.75	1.842	0.0142	0.8576	0.838	35.8	86.2	1.229	0.007
01	1.75	1.855	0.0122	0.8985	0.887	41.7	85.7	1.230	0.007
06	1.75	1.889	0.0138	0.9878	0.696	36.9	84.5	1.236	0.009
09	1.75	1.687	0.0175	0.2752	1.251	29.2	95.2	1.243	0.004
10	1.75	2.489	0.0317	2.944	0.481	16.1	65.0	1.254	0.015
Mean age ± 1σ			n=15	MSWD=3.53		33.7 ± 7.9		1.228	0.004
BR23-SD-3c, Sanidine, J=0.0004251±0.03%, IC=1.00376±0.0006249, NM-333A, Lab#=70963, Argus VI									
12	1.75	2.711	0.0516	4.358	0.126	9.9	52.5	1.105	0.044
02	1.75	3.158	0.0303	5.660	0.168	16.8	47.0	1.151	0.041
08	1.75	1.849	0.0161	1.189	0.329	31.8	81.0	1.160	0.016
09	1.75	1.835	0.0132	1.017	0.412	38.7	83.6	1.189	0.015
06	1.75	1.727	0.0174	0.6120	1.075	29.3	89.6	1.198	0.006
07	1.75	1.922	0.0247	1.204	0.247	20.6	81.5	1.214	0.021
04	1.75	2.223	0.0160	2.197	1.460	31.8	70.7	1.219	0.006
13	1.75	1.966	0.0184	1.327	1.888	27.7	80.1	1.219	0.005
03	1.75	2.252	0.0374	2.298	0.380	13.7	69.9	1.220	0.017
10	1.75	3.431	0.0129	6.275	0.406	39.4	45.9	1.221	0.022
01	1.75	2.041	0.0270	1.543	1.018	18.9	77.7	1.229	0.008
14	1.75	2.631	0.0221	3.522	1.570	23.1	60.4	1.232	0.009
05	1.75	1.801	0.0486	0.6969	0.467	10.5	88.7	1.238	0.011
11	1.75	3.226	0.0480	5.392	0.233	10.6	50.6	1.268	0.030
15	1.75	3.820	0.0467	5.736	0.883	10.9	55.6	1.650	0.013
Mean age ± 1σ			n=14	MSWD=3.74		23.1 ± 10.2		1.215	0.005

vii. Soda Dam Clast Age-Probability Spectrum

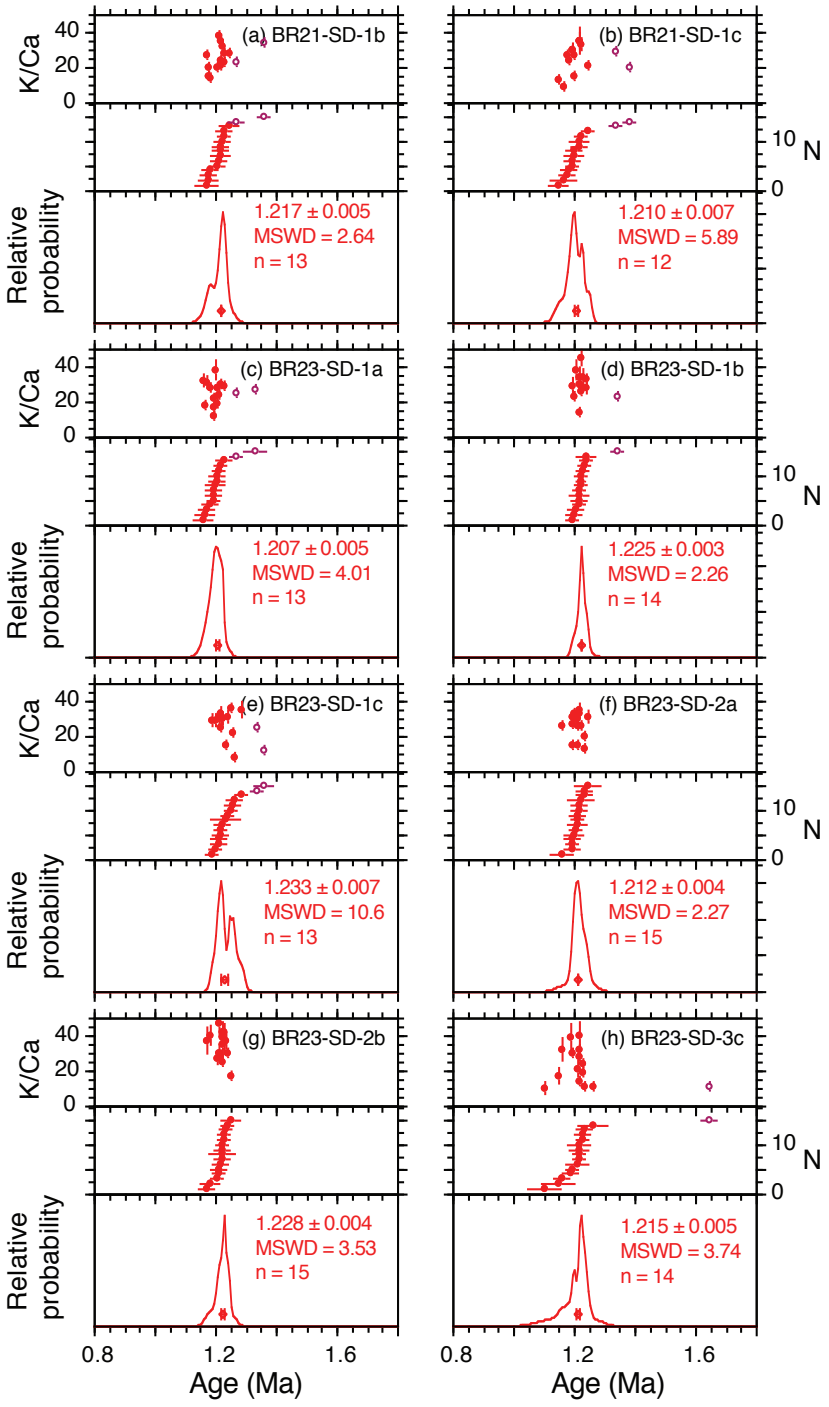

viii. Tephrochronology of Qt1 Terrace at La Junta

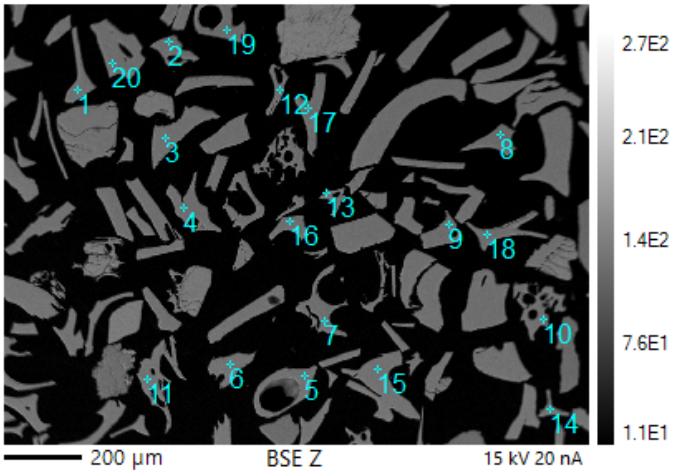

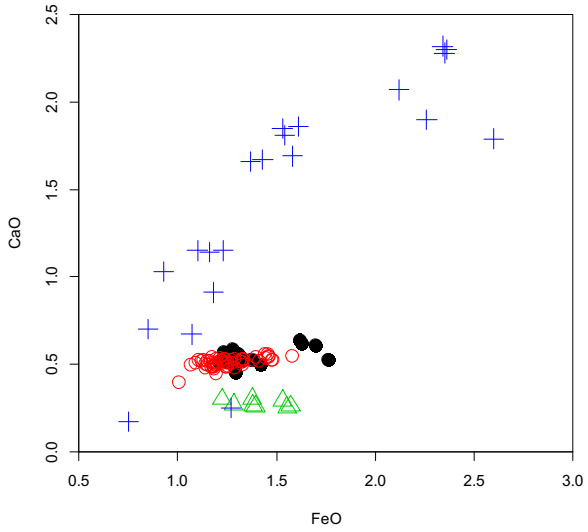

CR22G2

Lava Creek B and A (Lander, Wy)

Upper Bandelier

Tephra of the Parajito Plateau (Woldegabriel, et al 2007)

ix. Glass Tephrochronology Results

sample	P2O5	SiO2	SO2	TiO2	Al2O3	MgO	CaO	MnO	FeO	Na2O	K2O	F	Cl
NMASH-84-mean	0.01	77.02	0.01	0.07	12.21	0.00	0.26	0.04	1.57	3.80	4.49	0.22	0.31
NMASH-85-mean	0.02	76.49	0.01	0.05	12.18	0.00	0.25	0.10	1.55	4.29	4.50	0.20	0.35
NMASH-117-mean	0.02	76.75	0.02	0.05	12.08	0.01	0.30	0.05	1.38	4.22	4.52	0.19	0.31
NMASH-116-mean	0.01	77.45	0.02	0.03	11.89	0.17	0.29	0.05	1.53	3.66	4.52	0.08	0.33
NMASH-123-mean	0.01	77.52	0.00	0.06	12.20	0.01	0.27	0.06	0.98	3.72	4.93	0.06	0.169
NMASH-122-mean	0.01	77.82	0.01	0.06	11.95	0.01	0.29	0.05	0.98	3.58	4.98	0.05	0.207
NMASH-115-mean	0.01	77.71	0.01	0.09	12.21	0.04	0.35	0.07	0.77	3.56	5.05	0.00	0.136
NMASH-113-mean	0.02	77.91	0.01	0.10	12.00	0.02	0.34	0.03	0.77	3.62	5.01	0.04	0.126
NMASH-120-mean	0.01	76.23	0.02	0.06	13.24	0.06	0.59	0.03	0.73	4.33	4.54	0.03	0.128
NMASH-114-mean	0.01	77.68	0.02	0.11	12.38	0.04	0.37	0.04	0.78	3.39	5.01	0.04	0.125
NMASH-121-mean	0.01	77.37	0.01	0.12	12.30	0.16	0.38	0.05	0.77	3.53	5.08	0.06	0.162
NMASH-118-mean	0.02	77.21	0.01	0.09	12.24	0.06	0.28	0.04	1.28	3.43	5.23	0.01	0.094
NMASH-119-mean	0.01	75.07	0.01	0.08	14.21	0.02	0.32	0.05	0.71	3.95	5.46	0.03	0.095
CTR Stix 1990	0.00	77.13	0.00	0.09	12.50	0.07	0.41	0.06	0.95	3.68	5.11		
NMASH-83-mean	0.02	76.79	0.00	0.03	12.59	0.00	0.30	0.07	1.22	3.84	4.53	0.36	0.254
NMASH-86 mean	0.01	76.94	0.02	0.04	12.23	0.00	0.27	0.07	1.28	4.37	4.26	0.28	0.22
NMASH-87-mean	0.01	76.93	0.01	0.04	12.19	0.01	0.26	0.04	1.38	4.37	4.35	0.20	0.232
NMASH-88-mean	0.01	76.76	0.02	0.05	12.23	0.01	0.26	0.06	1.39	4.37	4.40	0.23	0.224
Pino1-mean	0.02	77.06	0.02	0.05	12.04	0.02	0.32	0.07	1.26	3.88	4.98	0.07	0.203
Pino2-mean	0.01	77.02	0.01	0.07	12.16	0.02	0.30	0.06	1.38	3.94	4.85	0.06	0.127

Pino3-Lt-mean	0.01	76.75	0.01	0.05	12.14	0.01	0.16	0.08	1.29	4.32	4.82	0.13	0.229
Guaje (Perkins, 1995)		77.18	0.00	0.07	11.93	0.03	0.27	0.07	1.38	4.01	4.75	0.13	0.169
NMASH average	0.02	76.99	0.01	0.18	12.71	0.16	0.81	0.04	0.87	3.07	4.91	0.15	0.072
NMASH-93-mean	0.03	75.56	0.00	0.25	13.50	0.24	1.17	0.05	1.23	3.47	4.36	0.07	0.069
NMASH-94-mean	0.01	77.19	0.01	0.16	12.70	0.09	0.68	0.03	0.81	3.58	4.63	0.05	0.057
NMASH 95-mean	0.03	75.91	0.01	0.23	13.33	0.17	0.93	0.04	1.07	3.72	4.44	0.07	0.07
NMASH-97-mean	0.04	76.39	0.01	0.20	13.04	0.15	0.77	0.02	1.02	3.47	4.70	0.13	0.069
NMASH-98-mean	0.04	75.49	0.02	0.24	13.39	0.25	1.08	0.01	1.20	3.55	4.61	0.05	0.072
NMASH-99-mean	0.05	75.92	0.02	0.22	13.03	0.17	0.91	0.04	1.19	3.54	4.78	0.08	0.06
NMASH-100-mean	0.03	74.78	0.02	0.23	13.65	0.24	1.21	0.03	1.23	3.88	4.61	0.02	0.075
NMASH-135 mean	0.01	76.63	0.01	0.05	12.46	0.00	0.26	0.06	1.31	4.13	4.51	0.30	0.246
NMASH-137-mean	0.01	76.86	0.01	0.10	12.36	0.02	0.24	0.04	1.09	3.71	5.33	0.08	0.151
NMASH-138-mean	0.01	76.68	0.01	0.06	12.59	0.01	0.32	0.04	1.07	4.08	4.88	0.13	0.129
NMASH-136-mean	0.14	70.09	0.02	0.57	15.58	0.83	2.33	0.05	2.63	3.88	3.73	0.06	0.092
SASS	0.01	73.96	0.01	0.07	11.56	0.01	0.27	0.05	1.22	3.82	4.76	0.13	0.143
SAP	0.01	73.81	0.00	0.05	11.54	0.01	0.28	0.07	1.23	3.73	4.96	0.10	0.139
LL23	0.01	73.70	0.01	0.03	11.45	0.01	0.27	0.08	1.33	3.99	4.60	0.21	0.252
LL07	0.01	73.37	0.01	0.05	11.15	0.00	0.27	0.08	1.46	4.12	4.22	0.32	0.27
BCT	0.01	73.64	0.01	0.08	11.36	0.01	0.29	0.06	1.33	3.80	4.65	0.15	0.18
LC	0.01	73.84	0.01	0.07	11.53	0.01	0.28	0.05	1.12	3.90	4.66	0.09	0.13
LBT1	0.01	73.51	0.02	0.04	11.49	0.01	0.24	0.08	1.25	4.01	4.64	0.28	0.19
LBT2	0.01	74.15	0.01	0.07	11.65	0.00	0.26	0.07	1.25	4.21	4.37	0.32	0.18
LBT3	0.02	74.05	0.01	0.06	11.60	0.00	0.27	0.07	1.24	4.30	4.38	0.14	0.16
UBT4	0.01	73.42	0.01	0.05	11.41	0.01	0.26	0.06	1.37	4.33	4.22	0.33	0.27

CDM	0.02	76.01	0.00	0.10	12.30	0.03	0.36	0.05	0.95	4.27	4.66	0.14	0.12
BSRP	0.01	73.18	0.01	0.19	12.11	0.13	0.87	0.05	0.68	3.43	4.55	0.04	0.07
BSRF	0.04	73.37	0.02	0.23	12.56	0.11	0.85	0.04	0.67	3.12	5.44	0.06	0.07
EC	0.04	74.33	0.01	0.16	12.05	0.09	0.75	0.04	0.78	3.40	4.65	0.05	0.07
BB	0.03	76.49	0.00	0.14	12.48	0.07	0.63	0.02	0.63	3.65	4.82	0.08	0.06
BCT (Check)	0.01	73.64	0.01	0.08	11.36	0.01	0.29	0.06	1.33	3.80	4.65	0.15	0.18
NQ	0.03	76.41	0.01	0.10	12.90	0.15	0.85	0.04	0.95	3.63	4.75	0.10	0.085
Lava Creek B (YS55)	0.01	76.29		0.16	12.65	0.03	0.45	0.02	1.53	3.62	5.24		
Lava Creek A (YS4)	0.02	76.88		0.14	12.58	0.15	0.27	0.03	1.50	3.35	5.07		
TC92-71		75.45		0.31	12.10	0.11	0.92	0.03	2.38	2.92	5.64	0.09	0.042
TC90-20		75.49		0.31	12.08	0.10	0.81	0.03	2.12	2.71	6.25	0.06	0.031
TC90-17		76.09		0.31	12.12	0.13	0.77	0.03	2.10	2.53	5.80	0.12	0.021
TC92-15c		75.39		0.33	12.01	0.10	0.87	0.03	2.25	2.72	6.16	0.11	0.021
TC89-36a		76.62		0.35	12.30	0.01	0.31	0.02	0.96	2.71	6.57	0.11	0.031
TC89-34a		76.07		0.33	11.98	0.09	0.84	0.04	2.35	2.31	5.78	0.19	0.02
TC89-33b		76.60		0.20	11.98	0.03	0.65	0.03	1.95	2.52	5.78	0.21	0.04
TC89-31a		76.40		0.20	12.05	0.03	0.66	0.03	1.96	2.52	5.87	0.23	0.042
TC89-28a		75.8855		0.3184	12.0992	0.1167	0.775	0.042	2.02	2.65	5.94	0.13	0.021
TC89-27c		76.56829		0.2098	11.9572	0.0524	0.608	0.031	1.81	2.31	6.19	0.22	0.042
TC89-25a		76.56033		0.2412	11.956	0.0734	0.577	0.031	1.72	2.2	6.4	0.21	0.031
TC89-24a		75.90468		0.3392	12.0854	0.117	0.742	0.032	1.94	2.44	6.25	0.13	0.021
TC89-21b		75.815		0.272	11.905	0.0731	0.73	0.042	1.99	2.3	6.79	0.052	0.0313
TC89-21a		76.08871		0.256	11.9355	0.0639	0.64	0.04	1.96	2.34	6.5	0.14	0.0320
TC89-19b		76.72		0.25	12.00	0.09	0.55	0.02	1.48	1.89	6.84	0.13	0.03
TC89-18a		76.19		0.21	11.95	0.06	0.61	0.03	1.76	2.39	6.44	0.29	0.05
TC89-17a		75.96		0.28	12.29	0.13	0.69	0.03	1.68	2.00	6.72	0.18	0.04
TC89-16a		76.72		0.23	11.98	0.08	0.55	0.02	1.48	1.79	6.94	0.18	0.032
TC89-15		76.70		0.23	12.01	0.08	0.58	0.02	1.54	1.48	7.06	0.25	0.042
TC89-12		76.14		0.18	12.19	0.06	0.53	0.03	1.39	1.92	7.27	0.21	0.064
TC89-20a		76.30		0.18	11.94	0.04	0.56	0.03	1.60	1.69	7.40	0.19	0.063
TC90-40		76.19		0.11	11.96	0.02	0.58	0.02	1.54	1.59	7.62	0.26	0.106
TC92-135		76.07		0.25	11.74	0.05	0.67	0.03	2.10	1.49	7.36	0.21	0.032

Lava Creek B (sample from G. Smith, analyzed at NMT)													
ak535-1	0.00	75.73	0.00	0.10	12.31	0.03	0.50	0.00	1.50	3.56	5.11	1.01	0.16
ak535-2	0.00	76.28	0.02	0.15	12.22	0.00	0.55	0.00	1.70	3.61	5.24	0.10	0.115
ak535-3	0.00	76.30	0.00	0.07	12.54	0.00	0.49	0.00	1.25	3.72	4.97	0.43	0.23
ak535-4	0.04	76.34	0.00	0.14	12.29	0.00	0.53	0.07	1.68	3.59	5.15	0.05	0.12
ak535-5	0.08	75.18	0.01	0.21	12.73	0.00	0.56	0.05	1.82	3.42	5.66	0.16	0.107
ak535-6	0.01	76.42	0.00	0.08	12.41	0.00	0.49	0.00	1.33	3.59	5.24	0.23	0.168
ak535-7	0.00	76.57	0.00	0.07	12.57	0.03	0.46	0.07	1.38	3.71	4.85	0.15	0.148
ak535-8	0.00	76.31	0.00	0.14	12.43	0.00	0.48	0.00	1.46	3.60	5.25	0.18	0.147
ak535-9	0.04	76.25	0.00	0.06	12.46	0.00	0.49	0.06	1.35	3.58	5.33	0.20	0.15
ak535-10	0.00	76.49	0.02	0.13	12.47	0.03	0.51	0.00	1.45	3.62	5.15	0.00	0.136
mean	0.02	76.19	0.01	0.12	12.44	0.01	0.51	0.03	1.49	3.60	5.19	0.25	0.147
ak594-1	0.01	75.68	0.00	0.16	12.65	0.03	0.49	0.00	1.57	3.62	5.44	0.24	0.096
ak594-2	0.01	76.03	0.00	0.10	12.73	0.00	0.57	0.00	1.48	3.89	4.85	0.21	0
ak594-3	0.00	75.70	0.03	0.19	12.49	0.01	0.58	0.00	1.74	3.59	5.42	0.15	0
ak594-4	0.01	75.52	0.00	0.11	13.13	0.00	0.52	0.01	1.31	3.71	5.19	0.27	0.18
ak594-5	0.00	75.84	0.02	0.13	12.73	0.01	0.58	0.03	1.73	3.39	5.32	0.13	0.10
ak594-6	0.04	75.69	0.03	0.10	12.59	0.00	0.57	0.00	1.70	3.50	5.54	0.15	0.10
ak594-7	0.00	76.38	0.00	0.11	12.31	0.01	0.53	0.00	1.39	3.64	5.27	0.21	0.16
ak594-8	0.00	76.74	0.02	0.09	12.28	0.00	0.50	0.04	1.35	3.55	4.96	0.29	0.16
ak594-9	0.02	76.08	0.02	0.11	12.43	0.00	0.49	0.06	1.29	3.64	5.30	0.31	0.21
ak594-10	0.00	76.08	0.00	0.07	12.60	0.02	0.55	0.01	1.31	3.89	5.10	0.25	0.13
mean	0.01	75.97	0.01	0.12	12.59	0.01	0.54	0.02	1.49	3.64	5.24	0.22	0.14
scd2-lcb-mean	0.01	76.58	0.01	0.10	12.37	0.01	0.51	0.01	1.46	3.51	5.09	0.19	0.13
Lava Creek B Izett 1981	0.00	76.54	0.00	0.13	12.35	0.08	0.59	0.04	1.47	3.16	5.64		
Lava Creek B (Perkins, 1995)		77.15	0.00	0.13	12.11	0.02	0.54	0.04	1.58	2.92	5.22	0.15	0.14
NMASH-75-mean	0.00	77.90	0.01	0.06	12.36	0.03	0.41	0.02	0.67	3.54	4.85	0.08	0.07
NMASH-76-mean	0.02	78.07	0.00	0.07	12.49	0.01	0.41	0.02	0.65	3.62	4.48	0.07	0.08

NMASH-77-mean	0.02	77.82	0.00	0.06	12.50	0.02	0.39	0.01	0.69	3.49	4.86	0.05	0.08
NMASH-78-mean	0.01	77.83	0.01	0.06	12.48	0.02	0.41	0.05	0.67	3.65	4.59	0.13	0.08
NMASH-79-mean	0.02	77.83	0.00	0.07	12.52	0.02	0.42	0.00	0.68	3.58	4.66	0.12	0.08
NMASH-80-mean	0.01	77.90	0.01	0.07	12.57	0.02	0.42	0.04	0.66	3.44	4.70	0.05	0.09
NMASH-81-mean	0.01	77.84	0.00	0.08	12.55	0.02	0.41	0.01	0.73	3.54	4.66	0.05	0.08
NMASH-82-mean	0.01	77.98	0.01	0.04	12.51	0.02	0.39	0.02	0.67	3.39	4.82	0.07	0.07
Bishop (Perkins, 1995)		78.16	0.00	0.05	12.58	0.03	0.44	0.03	0.69	3.22	4.68	0.04	0.08
Huckleberry Ridge (Perkins, 1995)		76.40	0.00	0.11	12.20	0.02	0.59	0.04	1.59	3.54	5.11	0.24	0.15
Kilgore (Perkins, 1995)		77.58	0.00	0.17	12.30	0.07	0.55	0.03	0.39	3.48	5.33	0.02	0.07
Walcott (Perkins, 1995)		77.87	0.00	0.19	12.09	0.08	0.50	0.04	0.20	3.47	5.36	0.09	0.11
Blacktail Creek (Perkins, 1995)		77.25	0.00	0.20	11.82	0.07	0.48	0.04	1.19	3.11	5.70	0.00	0.13
NMASH-124-mean	0.02	77.79	0.01	0.11	12.68	0.04	0.34	0.05	0.62	2.49	5.66	0.09	0.09
NMASH-125-mean	0.01	77.67	0.01	0.12	12.62	0.04	0.35	0.05	0.58	2.10	6.31	0.04	0.10
East Grants Ridge (Woldegabriel et al., 1995) GR95-11	0.01	76.20	0.01	0.03	13.57	0.00	0.48	0.11	0.71	4.08	4.41	0.36	0.02
East Grants Ridge (Woldegabriel et al., 1995) GR95-15	0.01	76.02	0.01	0.03	13.40	0.00	0.46	0.12	0.71	4.10	4.65	0.49	0.00
Lake	0.01	76.75	0.00	0.00	13.06	0.00	0.34	0.10	0.69	4.56	4.03	0.42	0.02
Lander Airport	0.01	76.76	0.00	0.06	12.13	0.00	0.52	0.03	1.25	3.95	4.87	0.21	0.20
YS4-LCA	0.02	76.88		0.14	12.58	0.15	0.27	0.03	1.5	3.35	5.07		
YP750-LCA	0.07	77.36		0.13	12.24	0.12	0.28	0.01	1.23	3	5.53		
YS8-LCA	0.02	77.89		0.1	12.6	0.07	0.24	0.02	0.9	3.33	4.84		

Simon Canyon-AT	0.00	77.30	0.01	0.09	12.67	0.05	0.48	0.06	0.52	4.13	4.57	0.07	0.06
Simon-Cyn-ash	0.00	77.12	0.01	0.08	12.13	0.03	0.31	0.06	1.21	4.04	4.72	0.13	0.14
CR-22-G2	**0.003**	**76.66**	**0.02**	**0.098**	**12.39**	**0.003**	**0.54**	**0.04**	**1.37**	**3.52**	**4.93**	**0.21**	**0.193**
SM-5	0.02	76.7		0.12	12.77	0.27	0.59	0.06	0.91	3.79	4.78		
SM-6	0.02	75.6		0.13	13.28	0.34	0.65	0.06	0.98	4.01	4.89		